LAWRENCE
LIVERMORE
NATIONAL
LABORATORY

LLNL-BOOK-591732

Nuclear Fission

J. Randrup, R. Vogt

October 15, 2012

100 Years of Subatomic Physics

Disclaimer

Publishers' page

Publishers' page

Publishers' page

Publishers' page

Contents

Chapter 11

Nuclear Fission

11.1 Introduction

Nuclear fission, the division of a nucleus into two parts, is a subatomic phenomenon that has influenced society profoundly. It may happen spontaneously or can be induced in a variety of ways. The possibility of such a process was totally unexpected and its discovery came as a shock to the scientific community. Nevertheless, once the existence of fission was established experimentally, it took a remarkably short time to put this spectacular process to practical use.

In this Chapter we do not intend to give a full review of the broad field of fission but focus on the most studied fission processes, namely spontaneous and neutron-induced, while we largely omit other active areas, such as heavy-ion induced fission, photofission, and delayed fission. Neutron-induced fission is useful for a variety of applications, while spontaneous fission, particularly of ^{252}Cf, is often used for calibration in fission measurements. Consequently there exist a wider range of data on these types of fission, from fragment information to measurements of associated neutrons and photons, and the field is experiencing worldwide activity.

Although nuclear fission has been studied intensely for over seventy years, it is still not well understood in detail and it remains an active field at the forefront of modern physics. First we recount briefly the discovery of fission and then describe the basic features of the phenomenon. Subsequently, we discuss the various experimental observables through which we may learn about the process. We then give an overview of fission modeling, both the formal treatment of the fission process itself and the phenomenological modeling of fission and its companion processes. Finally, we briefly discuss a number of new fission experiments that are underway.

11.1.1 *Discovery of fission*

The developments leading to the discovery of nuclear fission form a rich and fascinating story that cannot be related in detail here. Many accounts have been given and we refer the interested reader to the excellent books by Richard Rhodes [1] and Abraham Pais [2], giving just a brief summary below.

The discovery of the atomic nucleus in 1911 by Rutherford [3], a Nobel laureate already, is often taken as the start of the field of nuclear physics. But the nature of the nucleus remained a mystery for another two decades for the lack of means to probe it with, its positive electric providing an effective shield against exploration by means of charged particles, such as the α particle that had been used to reveal the existence of the nucleus. After a decade of worldwide radioactivity studies, Rutherford postulated that the nucleus contains two kinds of elementary particle (collectively called *nucleons*). It would have Z *protons*, each carrying one positive unit of electric charge, exactly the opposite of the electron's charge, and thus Z determines the chemical properties of that element. He further theorized, the nucleus would also contain a number, N, of elementary particles very similar to protons but electrically neutral, hence called *neutrons*. The neutron was subsequently identified in 1932, a decade later, by James Chadwick [4], a close associate of Rutherford.

Once discovered, the neutron was quickly turned into a useful tool in nuclear physics, the main advantage being that its electric neutrality enables it to readily enter the nucleus. In particular, Enrico Fermi and his colleagues in Rome undertook a systematic study in which they bombarded ever heavier elements with neutrons. Typically the target nucleus would absorb the neutron, thereby becoming radioactive, and the subsequent β decay would then lead to a nucleus having a charge number one unit larger than that of the bombarded element. However, bombarding uranium with neutrons in 1934, they obtained results that were difficult to interpret. After chemical analyses had shown that the resulting element could not be any known element above lead ($Z = 82$), Fermi believed that he had created a transuranic element with $Z = 94$ [5], a claim that was widely accepted at the time.

However, Ida Noddack, a German chemist and physicist, criticized Fermi's "proof" of transuranic element formation for its failure to eliminate *all* elements lighter than uranium, not only those with $Z \geq 82$ [6]. The paper is significant not only because she pointed out the flaw in Fermi's reasoning but also because she stated that *"it is conceivable that the nucleus breaks up into several large fragments, which would of course be isotopes of known elements but would not be neighbors of the irradiated element"*, thus presaging the concept of nuclear fission. However, because she did not suggest a theoretical basis for this possibility, which defied understanding at the time, her criticism was dismissed (and largely forgotten).

Fermi's publication spurred similar experiments in Berlin by Otto Hahn, Lise Meitner, and Fritz Strassmann. After Meitner, an Austrian Jew, lost her citizenship in 1938, she moved to Stockholm where she continued to collaborate with Hahn by mail and through his visits. In December 1938, Hahn and Strassmann sent a manuscript to Naturwissenschaften reporting they had detected the element barium after bombarding uranium with neutrons [7] and they simultaneously communicated this to Meitner. She and her nephew, Otto Frisch, who was working at Niels Bohr's institute in Copenhagen at the time, were spending the holiday break in the Swedish countryside when she received the letter from Hahn. This finding was astounding

because the mass of barium ($Z = 56$) is only about 60% of the uranium mass and no previously known type of nuclear transmutation could account for such a radical change of mass. Although Frisch was skeptical, Meitner trusted the abilities of Hahn who was using a well-established technique developed by Marie Curie.

To explain the result, Meitner and Frisch [8] invoked suggestions by George Gamow [9] and Niels Bohr [10] that the nucleus could be described as a liquid drop. After being agitated, such a nuclear drop would execute continual shape oscillations and thus, if becoming sufficiently deformed, it might break apart into two separate, necessarily smaller, nuclear drops. Simple estimates of the balance between the restoring effect of the surface tension and the disruptive tendency of the electric charge revealed that it would take only a small degree of agitation, similar to that caused by the absorption of a neutron, to enable the nucleus to split apart (see below). Meitner was furthermore able to explain the large energy release, approximately 200 MeV, as the difference between the mass of the original uranium nucleus and the sum of the two resulting lighter nuclei, making use of the mass-energy equivalence discovered by Albert Einstein [11], $E = Mc^2$. They also found that this amount of energy agrees well with the kinetic energy gained by the two product nuclei as a result of their being accelerated by their mutual Coulomb repulsion after their initial formation. Thus Meitner had correctly interpreted Hahn's results to mean that the uranium nucleus had roughly split in half. To bring out the analogy to binary fission of cells in biology, Frisch suggested calling the process "nuclear fission", a term that was generally adopted.

Following nearly five decades of work on radioactivity, the news of nuclear fission spread rapidly and many groups were soon conducting their own fission experiments. The interpretation by Meitner and Frisch of the phenomenon as nuclear fission was confirmed experimentally by Frisch already in January 1939 [12].

These experiments, which were being conducted at the verge of World War II during a period when many nuclear scientists, particularly in Germany and Italy, were being displaced by their racial heritage or their moral convictions, soon suggested a number of practical applications, the most prominent ones being power generation and explosives. (An annotated bibliography covering a broad range of nuclear issues is available at the Alsos Digital Library for Nuclear Issues: `alsos.wlu.edu`.) In 1939, the groups around Fermi, now at Columbia University in New York, and Frederic Joliot-Curie, in Paris, both discovered that neutron-induced fission of uranium resulted in the emission of several neutrons, in addition to the two product nuclei. Leo Szilard, a Hungarian physicist who had emigrated to the United States and was working with Fermi, immediately realized that neutron bombardment of uranium could lead to a sustained nuclear chain reaction with a tremendous energy output and he urged both groups not to publish their findings lest the Nazis should become interested. Fermi then refrained from publication, but Joliot-Curie reported his team's results in Nature [13]. This was the first of many attempts to limit the dissemination of basic scientific facts about nuclear fission.

11.1.2 *Basic features of fission*

It was recognized from the outset [14, 15] that the fission process can be regarded as an evolution of the shape of the agitated nucleus, see Fig. 11.1. The most basic features of fission can then be understood by considering the nucleus as a uniformly charged incompressible liquid drop. Its deformation-dependent energy is the sum of surface and Coulomb energies, $E(\varepsilon) = E_S(\varepsilon) + E_C(\varepsilon) = E_S^0 B_S(\varepsilon) + E_C^0 B_C(\varepsilon)$ where the deformation parameter ε characterizes the shape; the spherical shape has the surface energy $E_S^0 = a_S A^{2/3}$ (with $a_s \approx 18$ MeV) and the Coulomb energy $E_C^0 = a_C Z^2/A^{1/3}$ (with $a_c \approx 0.72$ MeV). Generally, the surface energy increases as the nucleus is distorted because of the associated increase of the surface area, while the Coulomb energy decreases because the charge becomes less concentrated. The result of these two opposite effects can be quantified by considering a slightly prolate spheroid of eccentricity e. It is elementary to show that $B_S(e) \approx 1 + \frac{2}{45}e^2$ and $B_C(e) \approx 1 - \frac{1}{45}e^2$, so the deformation energy $E_{\rm def}(e) \equiv E(e) - E(0)$ is given by

$$E_{\rm def}(e) \;=\; E_S^0[(B_S(e)-1) + 2x(B_C(e)-1)] \approx \tfrac{2}{45}E_S^0[1-x]e^2 \;, \qquad (11.1)$$

where the *fissility* parameter $x \equiv E_C^0/2E_S^0 = (a_C/2a_S)Z^2/A$ governs the degree of instability. For lighter nuclei, the fissility is relatively small and the nucleus will have a sizable fission barrier. But x increases steadily as one moves to heavier nuclei and the fission barrier grows ever smaller in both height and width and, accordingly, it will require correspondingly less agitation for the nucleus to overcome the barrier and undergo fission. Ultimately, for sufficiently heavy nuclei, the fissility becomes unity and the stability against deformation is lost altogether. This idealized analysis suggests that nuclei should loose stability against fission around $Z \approx 100$, as is indeed the case.

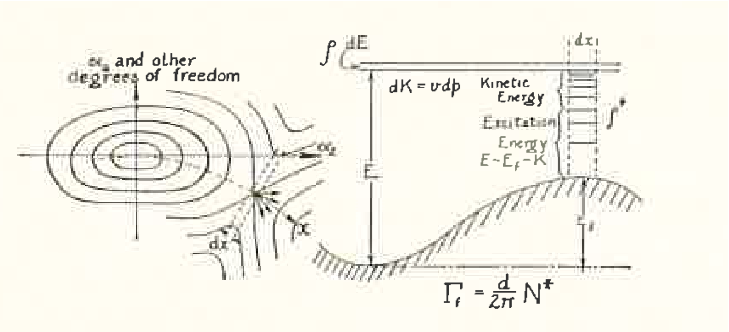

Fig. 11.1 *Left:* A schematic illustration of the potential energy contours associated with the deformation of the nuclear shape as a function of two deformation parameters; the resulting energy surface has a minimum around the ground-state shape and a saddle point at the critical deformation beyond which the nucleus will prefer to split into two fragments. *Right:* A cross section through the fission barrier showing also how the rate of decay can be calculated by statistical means. [From the early paper by Bohr and Wheeler [16].]

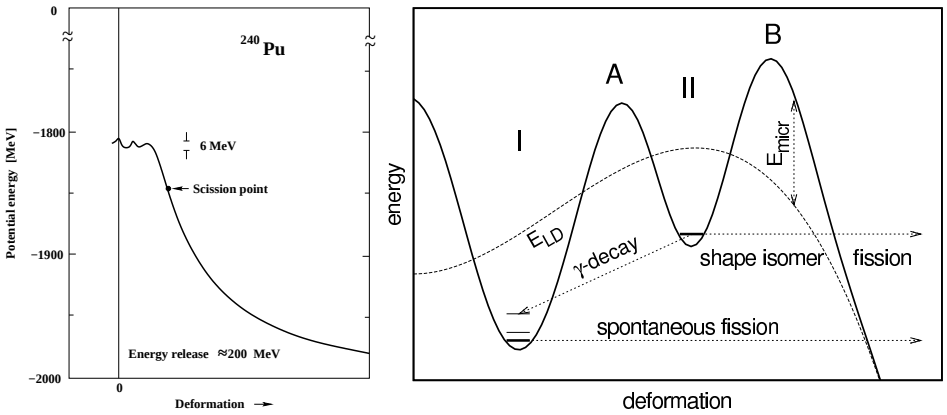

Fig. 11.2 *Left panel:* The general dependence of the potential energy on the fission degree of freedom for the nucleus ^{240}Pu. The smooth trends of the curve reflect the macroscopic behavior, which is dominated by the strong Coulomb repulsion between the two fragments, while the small wiggles arise from the microscopic (shell and pairing) corrections. From Ref. [17]. *Right panel:* Schematic plot of the double-humped fission barrier as function of the elongation. The ground state minimum (I), the first barrier (A), the isomeric minimum (II), and the second barrier (B) are marked. The dashed line shows the macroscopic part of the energy, while the solid line is the total energy obtained by including also the deformation-dependent shell and pairing corrections. From each of the two minima, the nucleus may fission by tunneling under the barrier; the isomeric state may also decay back to the ground state by γ emission. From Ref. [18].

The above simple analysis treats the nucleus as a macroscopic system whose energy changes smoothly with shape. This idealized picture is modified due to the microscopic structure of the nucleus. A given nuclear shape can be more or less accommodating to the individual nucleonic orbitals and, consequently, the resulting binding energy exhibits a shape-dependent oscillatory modification of the smooth macroscopic behavior. This is illustrated in the left panel of Fig. 11.2 which, for a typical actinide nucleus such as ^{236}U, shows how the smooth macroscopic deformation energy is modified as a result of the shell effects, leading to a double-humped fission barrier with a secondary minimum in which a long-lived shape isomeric state may be hosted.

Figure 11.3 calculated fission barriers for a number of even-even actinide nuclei, from ^{232}Th to ^{256}No. At the lower end of this region, the fissility is still somewhat below unity and there is a sizable macroscopic fission barrier. By contrast, x is very close to unity at the high end and there is hardly any macroscopic barrier left. Generally, the shell effects tend to increase the fission barrier height both because of the additional binding energy of slightly deformed shapes (which causes the ground states to be deformed) and because of the less favorable binding of the more deformed shapes in the saddle region. It should be noted that the very existence of the heaviest nuclei derives solely from such shell stabilization.

The present discussion of nuclear fission starts from an initially equilibrated nucleus. Such a nucleus can be prepared in a variety of ways. In the simplest case,

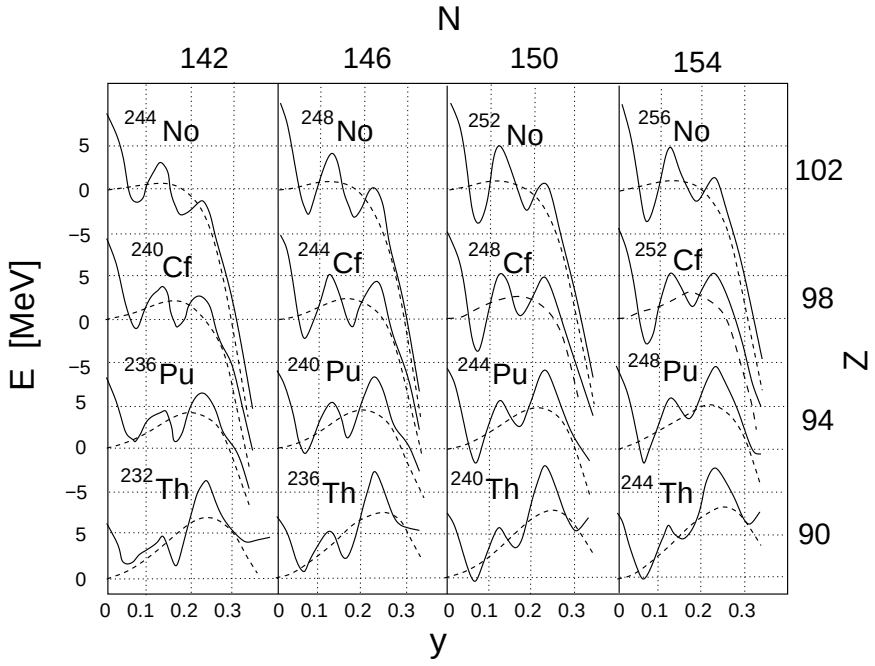

Fig. 11.3 Dependence of potential energy of actinide nuclei upon the symmetric-deformation coordinate (here called y). The dashed curves give the liquid-drop contributions and the solid curves the total potential energies, which are calculated with single-particle levels for ^{240}Pu. The dot-dashed curve for Th is calculated with single-particle levels for ^{228}Ra, and the dot-dashed curve for ^{256}No with levels for ^{258}Fm. The solid points at zero deformation are calculated with the appropriate spherical single-particle levels for each individual nucleus. From Ref. [17].

a nucleus may undergo spontaneous fission from its ground state (or an isomeric state) by quantum-mechanical tunneling through the fission barrier. Equilibrated compound nuclei can be prepared by absorption of neutron or light composite nuclei (^{2}H, ^{3}H, ^{3}He, ^{4}He, ...), by (complete or incomplete) fusion reactions, such as ^{48}Ca+^{208}Pb, or by electromagnetic means. As the reaction energy is increased, pre-equilibrium processes grow ever more important and may significantly influence the characteristics of the resulting compound nucleus, such as its mass number, excitation energy, and angular momentum.

If the fissionable nucleus is sufficiently excited, it may radiate neutrons or photons before fission occurs, leading to the terminology of *first-chance fission* for fission that is not preceded by any neutron emission, *second-chance fission* for fission preceded by the emission of one neutron, and so on. Such pre-fission emission processes generally cool the nucleus and may in fact de-excite it to such a degree that fission is no longer possible. But more typically, after the possible emission of one or more pre-fission neutrons, the nucleus will sooner or later find itself outside the fission saddle point and it will then proceed towards scission, the presumably relatively fast

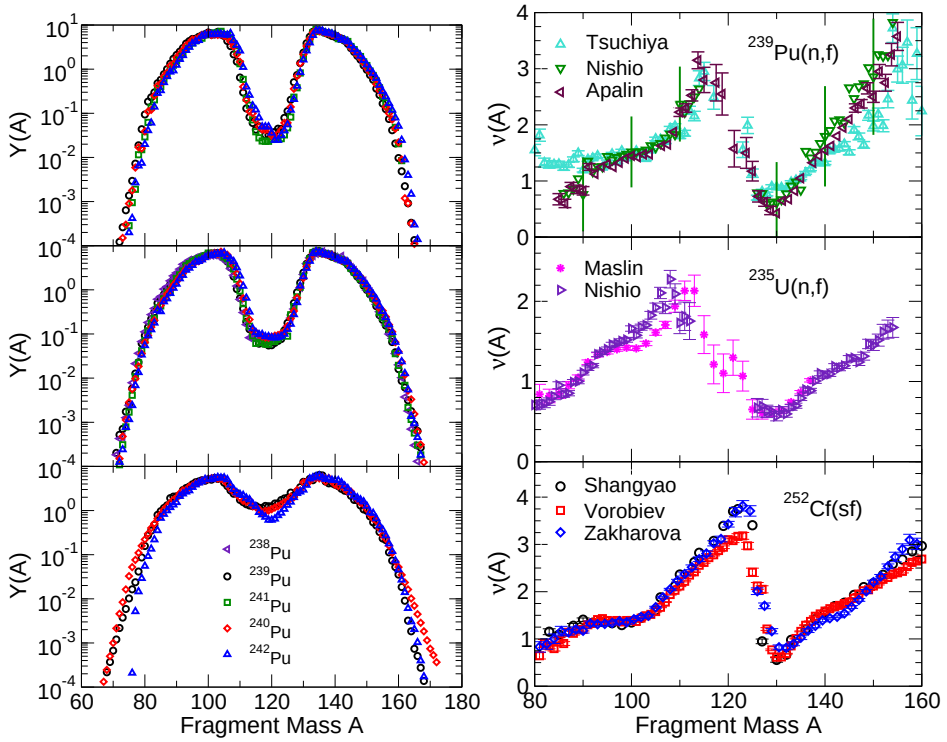

Fig. 11.4 *Left:* The fission product yields, given in percent, are shown for thermal-induced fission (*top*), 'fast' neutron-induced fission (*middle*), and 'high energy' neutron-induced fission (*bottom*) of several plutonium isotopes. In the top and middle panels, $Y(A)$ is shown for ^{238}Pu (◁), ^{239}Pu (○), ^{240}Pu (◇), ^{241}Pu (□), and ^{242}Pu (△), but only distributions for ^{239,240,242}Pu are available for high-energy incident neutrons. The data are all from the evaluation of Ref. [19]. *Right:* The measured average neutron multiplicity as a function of the fragment mass for ^{239}Pu(n,f) (*top*), ^{235}U(n, f) (*middle*), and ^{252}Cf(sf) (*bottom*). The data for ^{239}Pu($n_{\rm th}$,f) are from Refs. [20] (△), [21] (▽), and [22] ◁); the data for ^{235}U($n_{\rm th}$,f) are from Refs. [23] (∗) and [24] (▷); and the data for spontaneous fission of ^{252}Cf are from Refs. [25] (○), [26] (□), and [27] (◇).

process where the binary shape transforms itself into two separate receding fragments. There is evidence that neutrons or light nuclei may occasionally be emitted in conjunction with scission, but we shall leave this relatively rare phenomenon aside.

More prominent and, of much larger practical importance, is the remarkable fact that the fission fragment mass distributions are usually *not* centered around symmetry, a cause for great puzzlement during the early times of fission when the nucleus was thought to be a structureless liquid-drop-like system). The left-hand side of Fig. 11.4 shows the fragment mass yields for a number of plutonium isotopes. A closer inspection of these distributions (see later) reveals that fragments near $A = 132$ tend to be favored, a feature ascribed to the fact that $Z = 50$ and $N = 82$

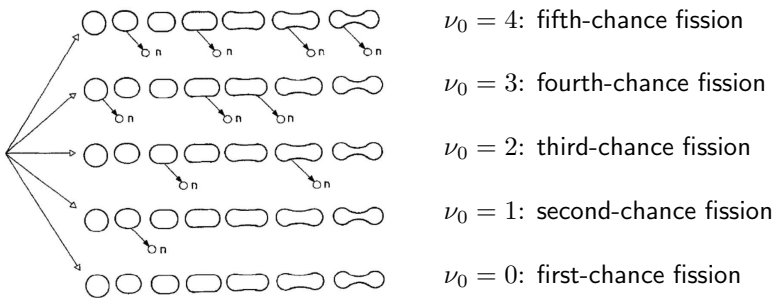

Fig. 11.5 Multi-chance fission: Starting from the same highly excited compound nucleus, the evolving system may emit a number of neutrons, ν_0, as it evolves towards scission, leading to 1^{st}-chance fission ($\nu_0 = 0$), 2^{nd}-chance fission ($\nu_0 = 1$), and so on. Adapted from Ref. [28].

are magic numbers with closed nuclear shells.

At the point of scission, each pre-fragment is significantly distorted relative to its ground-state shape due to the Coulomb force from the partner fragment. In addition, the pre-fragments have a large degree of statistical excitation. After the division has been completed and the two receding fragments are being accelerated by the mutual Coulomb repulsion, their shapes will relax towards their equilibrium forms, thus increasing the respective fragment temperatures. Typically, each fission fragment is sufficiently excited to evaporate one or more neutrons. Because the degree of fragment excitation depends somewhat on the shell structure, the same will be true for the average number of neutron evaporated. As well illustrated on the right-hand side of Fig. 11.4, the resulting fragment mass dependence of the (mean) number of evaporated neutrons exhibits a striking "sawtooth" behavior.

These evaporations cool the fission fragments and eventually lead to product nuclei that are no longer able to evaporate neutrons, their excitation energy being below the respective neutron separation energy. An excited product nucleus then de-excites towards its ground state by a cascade of photon emissions. The original fission fragments are usually formed with some amount of angular momentum, some of it due to a possible overall rotation of the fissioning nucleus but most of it usually imparted at the time of scission. Most of the original fragment angular momentum is still present in the the excited product nucleus. The photon emission will therefore tend to proceed in two stages: first the statistical excitation energy is radiated away, bringing the nucleus down near the so-called yrast line (where all its excitation energy is tied up in rotation) and then a sequence of coherent quadrupole quanta carry away the remaining angular momentum. Because these evaporation and radiation processes occur on a relatively short time scale, the resulting product nuclei are said to form the so-called *prompt* yield. Most of them are radioactive and will undergo (typically sequential) β decay on an ever slower time scale, contributing ultimately to the so-called cumulative yield.

11.2 Experimental observables

We discuss here the various fission stages in more detail, referring as much as possible to existing measurements without recourse to any particular model. In some cases, however, such as neutron emission prior to fission, we can only discuss the physics in terms of models because no reliable data are yet available.

11.2.1 *Pre-fission neutron emission*

At low incident neutron energies, below a few MeV, the neutron is absorbed into the target nucleus resulting in an equilibrated compound nucleus which may have a variety of fates. Most frequently it will fission directly. But, because the compound nucleus was formed by neutron absorption, it is energetically possible for it to re-emit a neutron. In that circumstance, the daughter nucleus cannot fission and will de-excite by sequential photon emission. While the likelihood for this is negligible for small incident energies, it grows appreciable as the neutron energy is raised above several MeV. Fission following such pre-fission evaporation is called multichance fission and is discussed below.

11.2.1.1 *Multichance fission*

As the energy of the incident neutron is raised, neutron evaporation from the produced compound nucleus competes ever more favorably with direct (first-chance) fission. The associated probability is given by the ratio of the fission and evaporation widths $\Gamma_{\rm f}(E^*)$ and $\Gamma_n(E^*)$, whose ratio can be estimated as [31]

$$\frac{\Gamma_n(E^*)}{\Gamma_{\rm f}(E^*)} \;=\; \frac{4\mu_n\sigma}{\pi\hbar^2}\frac{\int_0^{E_n}(E_n-E)\rho_n(E)dE}{\int_0^{E_{\rm f}}\rho_{\rm f}(E)dE}\;, \tag{11.2}$$

where $\mu_n = m_n(1-1/A)$ is the reduced neutron mass and $\sigma = \pi R^2 = \pi r_0^2 A^{2/3}$. Furthermore, $\rho_n(E)$ is the level density in the evaporation daughter nucleus at the excitation energy E, whose maximum value is given by $E_n = Q_n = E^* - S_n$, where Q_n is the Q value for neutron emission and S_n is the neutron separation energy. Similarly, $\rho_{\rm f}(E)$ is the level density of the transition configuration for the fissioning nucleus, *i.e.* when its shape is that associated with the top of the fission barrier; the excitation ϵ is measured relative to that barrier top, $B_{\rm f}$, so its maximum value is $E_{\rm f} = E^* - B_{\rm f}$.

The excitation energy of the evaporation daughter nucleus is $E_d^* = E^* - S_n - E$ where E is the kinetic energy of the relative motion between the emitted neutron and the daughter nucleus. If this quantity exceeds the fission barrier in the daughter nucleus, then second-chance fission is possible. The procedure described above may then be applied to the daughter nucleus, thus making further pre-fission neutron emission possible. Thus, as the incident neutron energy is raised, the emission of an ever increasing number of pre-fission neutrons becomes possible and the associ-

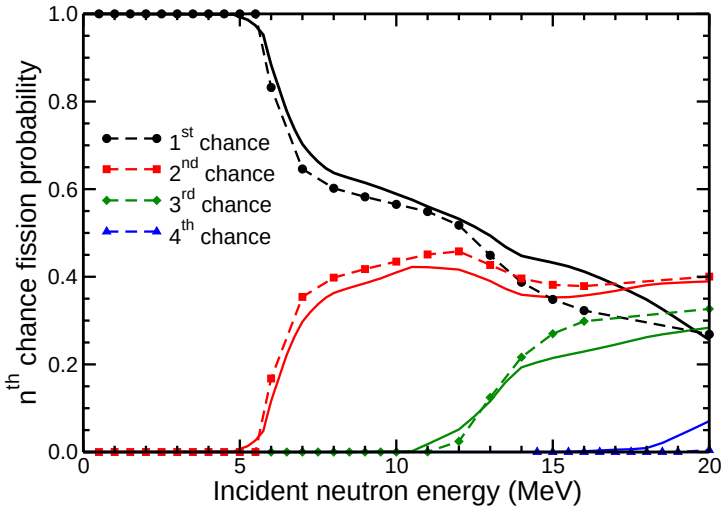

Fig. 11.6 The probability for first-, second-, third-, and fourth-chance fission as a function of incident neutron energy for ^{239}Pu(n,f). The solid curves show the `GNASH` results used in the ENDF-B/VII.0 evaluation [29], while the dashed curves with open symbols are the `FREYA` results. From Ref. [30].

ated fission events may be classified as first-chance fission (no pre-fission neutrons emitted), second-chance fission (one neutron is emitted prior to fission), and so on.

Figure 11.6 shows the probabilities for n^{th}-chance fission for incident neutron energies up to 20 MeV on ^{239}Pu, as obtained with the codes `GNASH` used in the ENDF-B/VII.0 evaluation [29] and the event-by-event generator `FREYA` [32]. The two calculations give rather similar results but, because these probabilities are not easy to measure experimentally, the accuracy of the calculations cannot be ascertained. Experimental information would clearly be valuable.

11.2.1.2 *Pre-equilibrium neutron emission*

At higher incident neutron energies, there is a growing chance that complete equilibrium is not established before the first neutron is emitted. Under such circumstances the calculation of statistical neutron evaporation must be replaced by a suitable non-equilibrium treatment. A variety of models have been developed for this process, see *e.g.* Ref. [33, 34].

The calculated probability for pre-equilibrium neutron emission is shown in the upper panel of Fig. 11.7 as a function of the incident neutron energy E_n. After being practically negligible below a few MeV, the probability for pre-equilibrium emission grows approximately linearly to about 24% at 20 MeV. The quantitative significance of pre-equilibrium emission is better seen by comparing the neutron spectrum obtained with and without the pre-equilibrium treatment, as shown in the lower panel of Fig. 11.7.

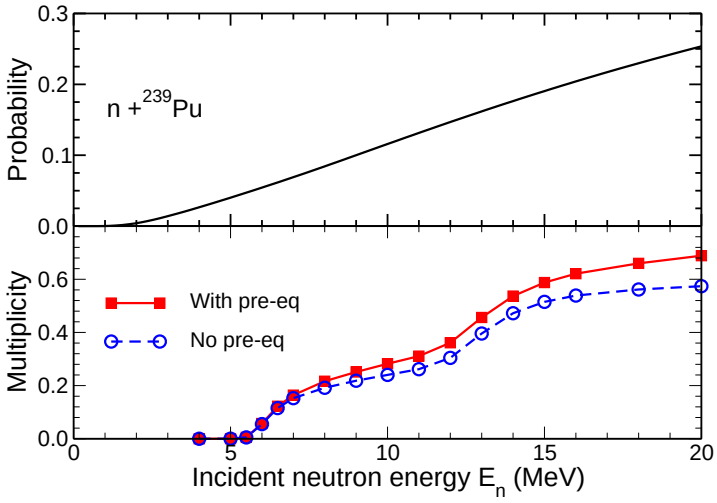

Fig. 11.7 *Top:* The probability for pre-equilibrium neutron emission as a function of the incident neutron energy for ^{239}Pu(n,f). *Bottom:* The corresponding average multiplicity of neutrons emitted prior to fission calculated without (dashed) and with (solid) the pre-equilibrium processes. From Ref. [30].

11.2.2 *Fragment observables*

We now discuss the characteristics of observables related to the fission fragments. Binary fission, resulting in two fragments, is dominant for neutron energies up to 20 MeV or so. Higher neutron energies may result in ternary or higher fission with more, lighter, fragments, but such events are relatively rare and are ignored for most applications. The fragments are (usually) of unequal size so one speaks of the heavy fragment and the light fragment; they have the mass numbers A_H and A_L, respectively. Typically the heavy fragment lies in the iodine-barium-lanthanum region, $130 \leq A_H \leq 145$, while the light fragment lies in the krypton-technetium-ruthenium region, $90 \leq A_L \leq 105$. The term 'fragment' usually refers to the two emerging nuclei prior to any neutron emission, while the neutron-evaporation residues are referred to as 'products'. For practical reasons, the measurements tend to determine the identity of one or both products so those of the original fragments must then be inferred from the associated neutron yields; when only the mean neutron multiplicity is known the determination of A_H and A_L is correspondingly uncertain. For the determination of the fragment kinetic energies it is helpful that the neutron evaporation affects the fragment motion only relatively little.

Earlier measurements used surface-barrier detectors [35] which employ a thin, solid material in which a track is etched when a charged particle passes through it. The timing tends to be rather slow and they are more subject to radiation damage than newer detector systems based on gas-filled ionization chambers [36]. The gas-filled chambers typically also have better energy resolution and subtend

a wider solid angle. In ionization chambers the gas is enclosed inside a chamber with conducting electrodes on either side of the chamber. The gas is ionized by the passage of charged particles and the ions drift to one side of the detector, while the dissociated electrons move to the opposite electrodes (a 'bias current' created by the applied voltage keeps the device from being saturated). More accurate tracks can be obtained using a time-projection chamber (TPC) [37] which applies a magnetic field in addition to the electric field. Thus modern detectors are capable of determining the charge, mass, kinetic energy, and direction of the emerging product nuclei.

11.2.2.1 *Fission fragment yields*

In experiments where the fission rate is low and the fragments can be identified individually, it is possible to determine the yields. While modern detectors make it possible to obtain $Y(A, Z)$, older experiments provide only $Y(A)$ or $Y(Z)$.

However, in circumstances where it is not possible to make immediate measurements, such as when examining bomb debris, the fission yield must be determined by radiochemical analysis. Because the fragments are neutron-rich, even after the prompt neutron emission, they are subject to β decay, ${}^{A}Z \rightarrow {}^{A}(Z-1) + e^{-} + \overline{\nu}$, which results in isobars with higher Z values but unchanged mass A. The chain of β decays continues until the product has become stable. A given stable isotope can be reached by decays from several original products, so the measurement of these isotopes does not give the direct fission yield but rather the *cumulative* yield of all fission products that lead to it. In radiochemical analyses, *independent* yields (yields produced directly by fission) are also very valuable. These may be obtained from very long-lived isotopes or from 'shielded' isotopes located immediately after a stable isotope so that they cannot result from β decay from the stable isotope but must arise directly from fission. It is preferable to measure both the cumulative yields, which are at the end of the decay chains and thus represent the yields of all isobars of mass A, as well as the independent yields. The yields appearing in the compilation by England and Rider [19] are cumulative yields while those obtained from experiments with fission chambers are typically independent yields because they are measured on shorter time scales than are usual for β decay.

The left-hand side of Fig. 11.4 shows the fission product yields as a function of the product mass number A for several different plutonium isotopes from ^{238}Pu to ^{242}Pu, all for fission induced by neutrons at various energies, namely 'thermal' ($E_n \approx 0.5$ MeV), 'fast' ($E_n \approx 1$ MeV), and 'high energy' ($E_n \approx 14$ MeV). Because the products are the residues after prompt neutron emission, the yield is not symmetric around $A = 120$.

The peaks of the heavy fragment yields tend to be anchored at $A = 132$ due to the doubly-magic spherical shell closure at $Z = 50$ and $N = 82$. and they therefore tend to change little with energy. But as the energy increases, the asymmetric yield peaks broaden and a central symmetric component appears ever more prominently.

The stability of the heavy fragment yields relative to the location of the light

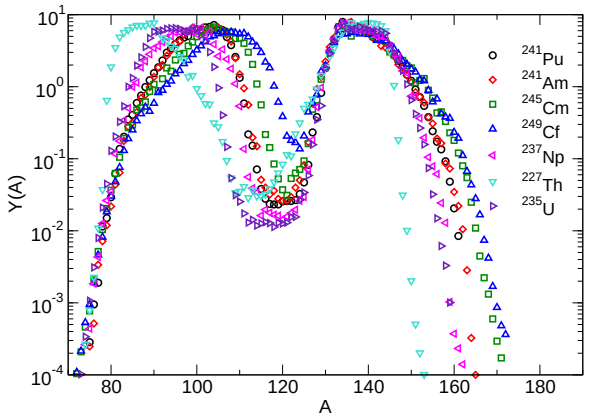

Fig. 11.8 The fission product yields, given in percent, are shown for thermal-induced fission of ^{241}Pu (○), ^{241}Am (◇), ^{235}Cm (□), ^{249}Cf (△), ^{237}Np (◁), ^{227}Th (▽), and ^{235}U (▷). The data are all from the evaluation of Ref. [19].

fragment peak is demonstrated in Fig. 11.8 where the product yields for thermal neutron-induced fission are shown for a variety of cases, from ^{227}Th to ^{249}Cf. All of the yields line up at $A \approx 132$ for the heavy fragment while the light fragment peak appears in the range $90 < A < 110$. The smaller the value of A, the larger the difference between the asymmetric peaks in the product yields. With a fixed point at $A \approx 132$, the lower the A value of the light fragment can be. We note that the yields for actinides with the same A_0 but different Z_0 are almost on top of each other, compare the yields for ^{241}Pu and ^{241}Am.

For energies above the fission barrier, where multichance fission becomes possible, the change in the yield curve is not straightforwardly due to the increased excitation energy of the system because of ever larger contributions from multichance fission Indeed, at $E_n \approx 14$ MeV it is more probable for one or more pre-fission neutrons to be emitted than none at all and consequently the fragment yield at 14 MeV is a composite distribution containing substantial contributions from second- and third-chance fission (see Fig. 11.6).

For a given fragment mass number A, the fragment charge Z displays a relatively narrow distribution of approximately Gaussian form. The associated dispersion is less than one unit (for example, $\sigma_Z = 0.4$ for ^{236}U* and $\sigma_Z = 0.5$ for ^{240}Pu* [38]).

11.2.2.2 *Fragment kinetic energies*

For a given partition of the total mass and charge among the two fragments, the Q value associated with that particular fission channel follows as the difference between the total mass A_0 of the fissioning nucleus and the ground-state masses of the two fragments,

$$Q_{LH} \;=\; M(^{A_0-\nu_0}Z_0^*) - M_L - M_H \;, \tag{11.3}$$

where ν_0 is the number of pre-fission neutrons emitted and the asterisk indicates that the fissioning nucleus is excited. This quantity is divided between the total kinetic energy (TKE) of the two emerging fission fragments and their total (combined) excitation energy (TXE). This latter quantity largely determines the number of post-fission neutrons emitted, $\nu = \nu_L + \nu_H$, and it is therefore, through energy conservation, expected that TKE is intimately related to ν.

Figure 11.9 shows the dependence of TKE on the fragment mass for several cases of both spontaneous and thermal neutron-induced fission. While the total kinetic energy of the two fragments can vary by as much as ≈ 25 MeV for the measurements shown, the general trends are the same in all cases, independent of whether the fission was induced or spontaneous. The left panel shows the measured average TKE as a function of A_H. Near symmetry, the plutonium fission fragments are mid-shell nuclei and thus subject to strong deformations. Consequently, the scission configuration will contain significant deformation energy and TKE will be correspondingly low. At $A_H \approx 132$, the heavy fragment is close to the doubly-magic closed shell and is therefore resistant to distortions away from sphericity [43]. Consequently, the scission configuration is fairly compact, causing the TKE to exhibit a maximum even though the complementary light fragment is far from a closed shell and hence significantly deformed.

The peak in TKE(A_H) at $A_H \approx 132$ is at the same point as the peak in the fission product yields for the heavy fragment, as shown previously. The drop in TKE at high A_H comes from the heavy fragment, as seen when the kinetic energies of single fragments are shown as a function of A, see Fig. 11.9. The light fragment carries away significantly more kinetic energy than the heavy fragment. Furthermore, the kinetic energy of the fragment is nearly constant for $A_f < 106$, but after the dip near symmetry it exhibits n approximately linear decrease.

Few data are available for above-thermal values of E_n. However, one expects

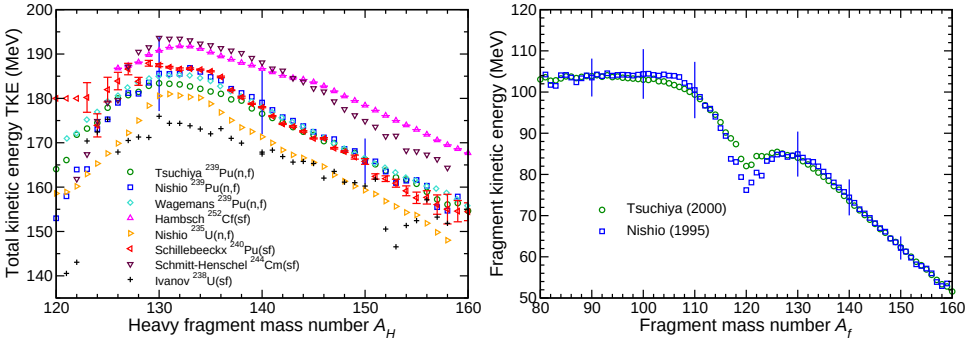

Fig. 11.9 The left-hand side shows total fragment kinetic energies as functions of the heavy fragment mass for ^{239}Pu($n_{\rm th}$,f) from Refs. [20] (○), [21] (□), and [39] (◇), ^{252}Cf(sf) [40] (△)^{235}U($n_{\rm th}$,f) [24] (▷), ^{240}Pu(sf) [41] (◁), ^{244}Cm(sf) [35] (▽), ^{238}U(sf) [42] (+). The right-hand side shows the average fragment kinetic energy as a function of fragment mass for ^{239}Pu($n_{\rm th}$,f) from Refs. [20] (○) and [21] (□).

the shape of TKE(A_H) to stay similar up to rather large values of E_n because shell effects remain significant as long as $E_n < 20 - 30$ MeV.

11.2.3 *Neutron observables*

The most interesting observables arising from fission are associated with the neutrons and photons emitted before and shortly after fission: the prompt neutrons and prompt photons. Here we describe several prompt neutron observables that have been measured.

11.2.3.1 *Multiplicity as a function of fragment mass*

The right-hand side of Fig. 11.4 shows the dependence of the neutron multiplicity, ν, on the fission fragment mass number, A. The function $\nu(A)$ exhibits a 'sawtooth' behavior: The neutron multiplicity from the light fragment increases slowly as A approaches $\frac{1}{2}A_0$ and then drops rather sharply to a minimum around $A_H \approx 132$, the same location as the maximum of TKE(A_H) [43]. Due to the presence of the closed shell at that point, the fragments are particularly resistant to neutron emission. The multiplicity again increases past the dip region. The dip tends to be more sharply defined for larger nuclei where $\frac{1}{2}A_0$ is close to 132. For example, the drop is particularly abrupt for ^{252}Cf where $\frac{1}{2}A_0 = 126$.

11.2.3.2 *Neutron multiplicity distribution*

Figure 11.10 shows the neutron multiplicity distribution $P(\nu)$ for several cases. Each emitted neutron reduces the excitation energy in the residue by not only its kinetic energy E ($\overline{E} = 2T$ where $T \approx 0.5 - 1$ MeV is the maximum temperature in the evaporation daughter) but also by the separation energy S_n (which is generally significantly larger, $S_n \approx 6$ MeV). Therefore the resulting $P(\nu)$ is narrower than a Poisson distribution with the same average multiplicity, as clearly seen.

In experiments, the quantity $P(\nu)$ is determined by detecting fission events in a sample of material and correlating these with simultaneous neutron detection. The relative probability for emission of ν neutrons in given event, $P(\nu)$, is inferred by combining the calculated probability for observing n neutrons when ν were emitted, $Q(n;\nu)$, with the detector efficiency determined from the count rate by comparison with a calibration source having a known $\overline{\nu}$; typically ^{252}Cf(sf) is used. Thus, while the value of $\overline{\nu}$ may be well measured for a given isotope, the distribution $P(\nu)$ is less well determined.

The results labeled 'Holden-Zucker' in Fig. 11.10 for ^{238}U(sf) are consensus values from a 1985 report by Holden and Zucker [44]. While results for the other cases are generally available from this reference, they are not shown if there is good agreement between the data displayed here and in Ref. [44] or if there are more recent data available.

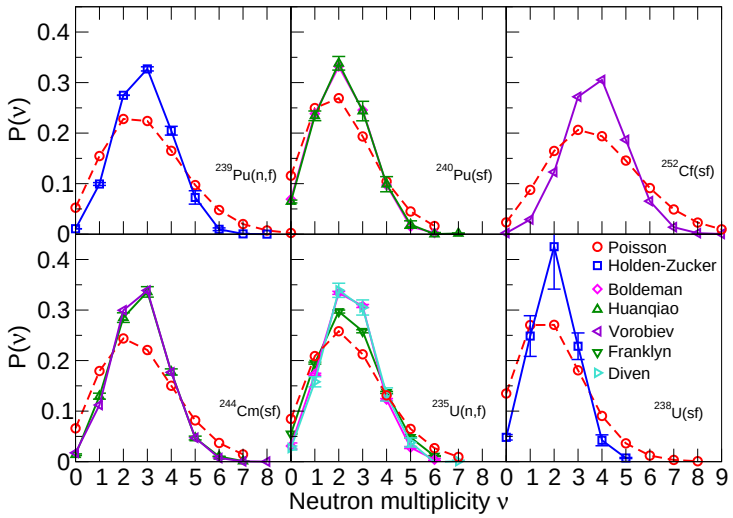

Fig. 11.10 The measured neutron multiplicity distribution, $P(\nu)$, compared to the corresponding Poisson distribution. The composite results of [44] (□) are shown for thermal neutron-induced fission of ^{239}Pu (*upper left*) and spontaneous fission of ^{238}U (*lower right*). Data from spontaneous fission of ^{240}Pu (*upper center*), Refs. [45] (△) and [46] (□); ^{252}Cf (*upper right*) [48] (◁); and ^{244}Cm (*lower left*) [45] (△) and [49] (▷). Data from thermal neutron-induced fission of ^{235}U (*bottom center*) [50] (▽), [51] (◊), and [52] (▷) are also shown.

11.2.3.3 *Energy dependence of neutron multiplicity*

As the energy of the incident neutron is increased, the resulting compound nucleus becomes correspondingly more excited. This in turn primarily increases the average number of neutrons evaporated both before and after fission, whereas there is little effect on the fragment kinetic energies. This latter feature is consistent with expectations based on the theoretical prediction that the dissipation associated with the nuclear shape evolution is fairly temperature independent [53]. (In fact, the fragment TKE decreases somewhat with E_n [54].) Furthermore, the neutron spectra harden slightly due to the increased fragment temperatures.)

The energy dependence of the average neutron multiplicity $\overline{\nu}$ is shown in Fig. 11.11 for a number of cases. These data are taken from the ENDF/B-VII database [29]; the energies at which evaluated data are available are indicated by symbols, though the 20 MeV point is often extrapolated rather than measured. Systematics are often used for cases where few data are available, such as ^{249}Cf(n,f).

There are, on average, more than two neutrons emitted in each case shown in Fig. 11.11. The number of neutrons emitted at thermal energies, $E_n \approx 0$, tends to increase with increasing nuclear charge Z. Note, for example, that while the A-dependent yields in Fig. 11.8 are almost identical for ^{241}Pu and ^{241}Am, the neutron multiplicity is higher for ^{241}Am ($Z = 95$) than for ^{241}Pu ($Z = 94$). On the other hand, the slope of $\nu(E_n)$ depends only weakly on Z. The outlying cases shown,

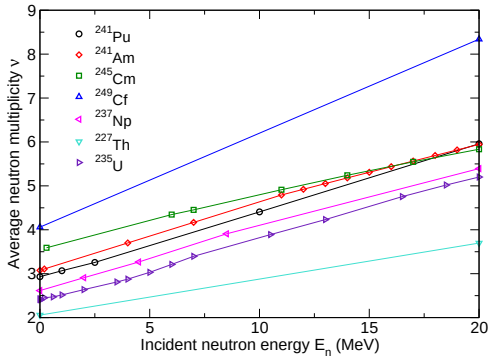

Fig. 11.11 The neutron multiplicity as a function of incident neutron energy, E_n, is shown for ^{241}Pu (○), ^{241}Am (◇), ^{235}Cm (□), ^{249}Cf (△), ^{237}Np (◁), ^{227}Th (▽), and ^{235}U (▷). The data are all from the evaluation of Ref. [29].

^{227}Th and ^{249}Cf, have no intermediate values of $\nu(E)$ between thermal neutrons and $E_n = 20$ MeV.

11.2.4 *Prompt fission neutron spectra*

The energy spectrum of the prompt fission neutrons are particularly important for practical applications, such as power generation. Because the spectra decrease several orders of magnitude in the energy range of interest ($E < 20$ MeV), both calculations and data are often shown relative to a Maxwellian distribution, $dN/dE = N_0\sqrt{E}\exp(-E/T)$, where the temperature parameter T is fixed to a given value. In the cases shown in Figs. 11.12 and 11.13, $T \approx 1.42$ MeV.

Figure 11.12 shows this ratio for experimental data obtained for thermal-neutron induced fission of ^{239}Pu from Refs. [55–57] and for $E_n = 0.5$ MeV from Ref. [58]. While the data are in general agreement for $1 < E < 5$ MeV, there are discrepancies between the data sets both at $E < 1$ MeV and $E > 5$ MeV. In the tail of the distribution, $E > 5$ MeV, three of the sets suggest a decrease relative to the Maxwellian, while the fourth, from Ref. [57], indicates an increase, albeit with large uncertainties. At the low-energy end of the spectrum, two of the data sets (Refs. [56, 57]) agree well with the Maxwellian. The remaining data sets are either high (Ref. [55]) or low (Ref. [58]) relative to the Maxwell distribution, albeit with significant uncertainties. Note that the most recent measurements were taken in 1995. Therefore, the field would benefit from more modern, high precision measurements.

Figure 11.13 shows the spectral ratios for ^{235}U(n,f) at several different values of E_n. In most cases, the data are mutually consistent within the uncertainties and they exhibit the same general trends. The most noticeable discrepancy occurs for $E_n = 14.7$ MeV which is above the threshold for multichance fission (the 2.9-MeV measurement made with the same apparatus is in good agreement with the

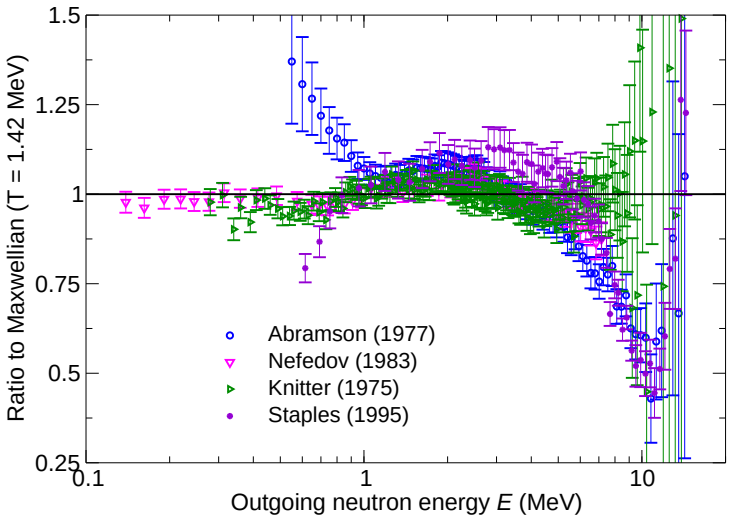

Fig. 11.12 Energy spectra of neutrons emitted from ^{239}Pu(n,f), taken from Refs. [55] (○), [56] (▽), [57] (▷)and [58] (•); shown relative to a Maxwell distribution having T=1.42 MeV.

Maxwellian for $E < 4$ MeV). The relative abundance of low-energy neutrons in the 14.7 MeV spectrum may be due to pre-fission neutrons which generally have lower average energy than those evaporated from fully accelerated fragments, Also noteworthy is the spectral spike at $E \approx 7$ MeV which is likely due to pre-equilibrium neutron emission. It appears at an energy equal to the difference between the incident neutron energy, E_n, and the height of the fission barrier, B_f, and the sharp drop above this energy is a reflection of energy conservation which prohibits emission of any pre-fission neutrons having energies greater than $E_n - B_\mathrm{f}$. Therefore, the tail of the spectral distribution results primarily from first-chance fission.

11.2.5 *Photon observables*

Measurements of prompt fission photons, especially in conjunction with neutron measurements, are particularly important for determining the total prompt energy release in fission and the average angular momentum of the fission fragments. Unfortunately, the experimental data on prompt photon fission observables are scarce and tend to be fairly old. Some of the available differential data are shown in Figs. 11.14 and 11.15. Nifenecker *et al.* [63] and Nardi *et al.* [64] reported results with a ^{252}Cf(sf) source, while Pleasonton *et al.* [62] employed thermal neutrons on ^{235}U. The Cf data sets above, both taken in the early 1970's, exhibit mutual contradictions that likely arise from both the experimental techniques and the assumptions in the analyses. These three measurements are described briefly below.

Pleasonton *et al.* [62] measured the average number N_γ and energy E_γ of photons as functions of fragment mass A and total kinetic energy TKE in ^{235}U(n_th,f). They

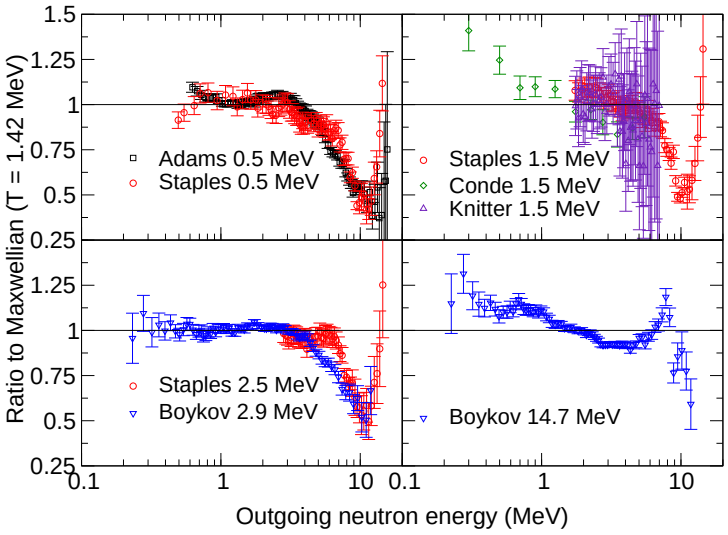

Fig. 11.13 In a presentation similar to Fig. 11.12 are shown the ratios of the neutron spectra for ^{235}U(n,f), taken from Refs. [59] (□), [60] (◇), [57] (△), [61] (▽), and [58] (○); the incident neutron energies $E_{\rm n}$ are indicated.

found that N_γ and E_γ increase slowly with heavy fragment mass (decrease with light fragment mass), as shown on the right-hand side of Fig. 11.14. They find a sawtooth shape similar to that seen in $\nu(A)$ but with the edge at $A \approx 125$. The shape of $N_\gamma(A)$ may suggest important neutron-photon competition. The average photon energy emitted by the light fragment is about 30% higher than that from the heavy fragment. The lower average value of $\langle E_\gamma \rangle_H$ indicates that the heavy fragment is created with greater initial angular momentum [62], in agreement with

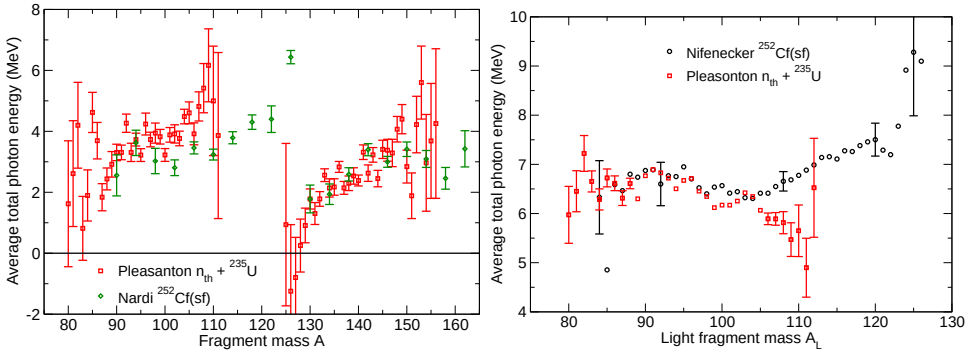

Fig. 11.14 The average total emitted photon energy is shown as a function of the fragment mass, A, (*left*) and light-fragment mass, A_L, (*right*). The squares show the data from Ref. [62] with thermal neutrons on ^{235}U, while the circles [63] and diamonds [64] show data taken on ^{252}Cf(sf).

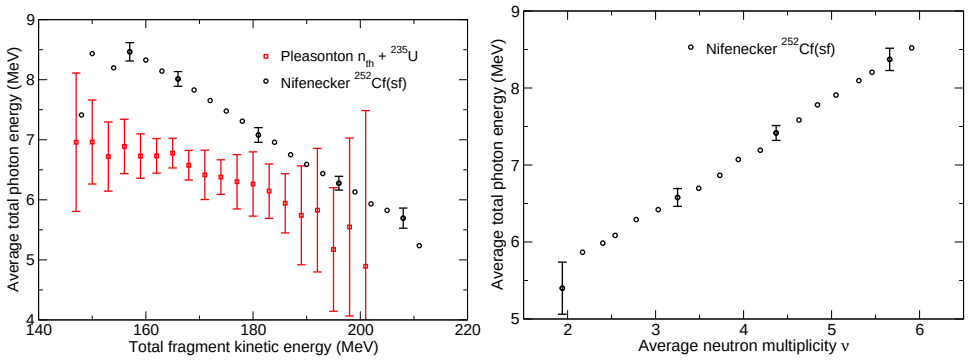

Fig. 11.15 *Left panel:* Average total emitted photon energy as a function of total fragment kinetic energy for ^{235}U($n_{\rm th}, f$) [62] (■) and ^{252}Cf(sf) [63] (●). *Right panel:* Average total emitted photon energy as a function of the average neutron multiplicity for ^{252}Cf(sf) reported in Ref. [63].

the results of Ref. [65]. The ratio E_γ/N_γ is highest near the doubly-closed shell at $A \approx 132$. Thus the smaller deformation of the heavy fragment, which reduces the probability for neutron emission, also allows fewer photons to be emitted without substantially changing the total photon energy.

The data also suggest a slow decrease of E_γ with TKE, shown on the left-hand side of Fig. 11.15. Higher TKE is associated with lower nuclear deformation (hence lower excitation energy). This is also consistent with the light fragment being more deformed with higher S for low TKE, while the heavy fragment is more deformed with higher S when TKE is high. Thus the angular momentum S is $\approx (0-2)\hbar$ near closed shells and $\approx 10\hbar$ for deformed fragments, giving an average of $S \approx 6.4\hbar$. Their TKE results are in relatively good agreement with the ^{252}Cf(sf) measurement of Nardi *et al.* [64] but not with that of Nifenecker *et al.* [63].

Nifenecker *et al.* measured both neutrons and photons emitted from ^{252}Cf(sf) to study the competition between neutron and photon emission [63]. They reported the average total photon energy as a function of the light fragment mass, A_L, shown on the right-hand side of Fig. 11.14, and total fragment kinetic energy, shown on the left-hand side of Fig. 11.15. The total photon energy increases almost linearly for $A_L > 100$ with an enhancement for $A_L \rightarrow 126$. They also observe a strong linear decrease in E_γ with TKE and they extract a linear increase in fragment angular momentum with E^*, $\overline{S}(E^*) = aE^* + S_0$ with $a \approx 0.2$ assuming that S changes by 2 units for every MeV of photon energy. Allowing an A dependence of the ground-state spin S_0, this relation can account for E_γ(TKE) in Fig. 11.15. They also find $E_\gamma = (0.75\,\nu + 4)$ MeV (see the right-hand side of Fig. 11.15 [63]). This is a rather striking positive correlation, if verified.

Earlier calculations [66] of the angular momentum acquired by the fragments through mutual Coulomb excitation at scission found that, for a given fragment deformation, the angular momenta increase rapidly with fragment kinetic energy, in contradiction with Nifenecker's conclusions [63]. Because Ref. [66] also suggested

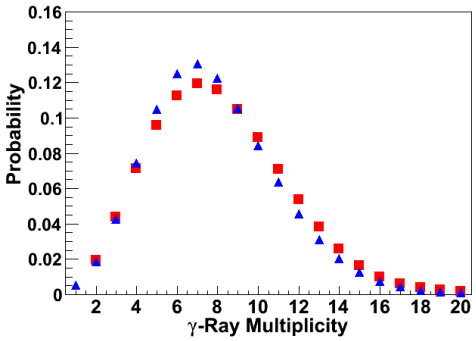

Fig. 11.16 The unfolded prompt photon multiplicity distribution for ^{252}Cf(sf) measured by DANCE (■) compared with the semi-empirical distribution of Brunson (▲), see Ref. [67].

that the fragment angular momentum increases with deformation energy, Niefenecker *et al.* concluded that the fragment deformation is the dominant determinant of its angular momentum. Because the rotational energy is only part of the total fragment excitation energy, the correlation between the deformation energy and TKE may be weaker than asserted in Ref. [63].

The ^{252}Cf(sf) measurement of Nardi *et al.* [64], which separated photons from neutrons using time-of-flight techniques, found a behavior of $E_\gamma(A)$ similar to that of Pleasonton *et al.* [62], see Fig. 11.14. Nardi *et al.* suggested that the behavior of $E_\gamma(A)$ and $E_\gamma(\nu)$ is due not to fragment angular momentum, as suggested by Niefenecker [63], but to the variation of neutron binding energy in the fragments. They ruled out any strong dependence of angular momentum with TKE (and thus with excitation) and obtain an upper limit on the magnitude of the effect of fragment angular momentum compatible with both the earlier ^{252}Cf(sf) result of Wilhelmy *et al.* [65] and the ^{235}U($n_{\rm th}$,f) result of Pleasonton *et al.* [62] which found S to be independent of TKE to within one unit. However, it strongly contradicts Niefenecker's result. New measurements of these observables, with modern detectors, would clearly be desirable.

Such new measurements are becoming available. Thus two results, from the DANCE Collaboration taking data at LANL [68] and the LiBerACE Collaboration [69] making measurements at LBNL, appeared recently, as is briefly discussed below.

The prompt photon energy and multiplicity distributions from ^{252}Cf(sf) was measured with a highly segmented 4π photon calorimeter, the Detector for Advanced Neutron Capture Experiments (DANCE) [68], together with a compact gas-filled parallel-plate avalanche counter [70]. Both the energy and multiplicity distributions were unfolded by simulating the detector response, employing a model validated by the photon calibration sources. The unfolded photon multiplicity distribution is shown in Fig. 11.16, together with the semi-empirical distribution by Brunson [71]. They agree reasonably well.

The Livermore-Berkeley Array for Collaborative Experiments (LiBerACE) uses ^{252}Cf(sf) to study photon multiplicity relative to neutron emission. The Cf source is surrounded with high-purity germanium detectors enclosed in bismuth-germanate detectors. The geometry provides good solid angle coverage. Room background, as well as photons from cosmic rays, were subtracted by counting photons with no source present. Two separate analyses were made, one of the overall photon multiplicity and the other of the photon multiplicity correlated with neutron multiplicity.

Because the background from photons emitted by β decays of fission products (delayed photons) at low multiplicities was indistinguishable from prompt fission photons, only detected photon multiplicities greater than seven were used in the analysis of the overall photon multiplicity. The measured multiplicity distributions were compared to both the Brunson distribution [71] shown in Fig. 11.16 and a Monte-Carlo calculation of statistical photon emission [72]. For multiplicities greater than seven, the measured distribution dropped off less rapidity than the calculations, with the Monte-Carlo result [72] dropping faster with multiplicity than the Brunson determination [71].

The second exploited the observation of discrete energy photons coming from known transitions in identified fission products, after neutron emission, to study neutron-photon correlations. Monte-Carlo calculations [72, 73] predict an anti-correlation between photons and neutrons, *i.e.* the average photon multiplicity decreases with increasing neutron multiplicity. Thus, if the average photon energy is independent of neutron multiplicity, higher photon multiplicities arise from higher fragment excitation energies. On the other hand, Niefenecker *et al.* [63] suggested that there was a positive correlation between neutron and photon multiplicities (see the right-hand side of Fig. 11.15), provided that the neutron contribution from recoil photons was subtracted correctly. This result was based on the fact that discrete photons can be separated from the background of statistical decays to the continuum and Compton scattering of high-energy photons. They chose two deformed even-even product pairs: ^{106}Mo+^{144}Ba, with two emitted neutrons (ν=2), and ^{106}Mo+^{142}Ba, with four neutrons emitted (ν=4). They then compared the photon multiplicity distributions from these product pairs with each other and with Monte-Carlo predictions [72]. If there is an anti-correlation between neutrons and photons, a backward shift in the centroid of the photon multiplicity distribution for four neutrons relative to two neutrons should be observed. But if there is a positive correlation, the centroid for four-neutron emission should be at higher photon multiplicity than for two-neutron emission. They observed no difference in the location of the centroids for the selected Mo+Ba ratios, within their significant statistical uncertainties, corresponding to no correlation between neutron and photon emission. However, it is important to remember that the Monte-Carlo results were based on an average of many fragment pairs, not only specific photon transitions in selected pairs. This issue is thus still open.

11.3 Modeling of fission

Nuclear fission is the result of a complicated dynamical evolution of a small many-body system in which quantum mechanics plays a major role. As such, fission presents many challenging issues that have not yet been satisfactorily elucidated, even after many years. We cannot here fully review all the various theoretical approaches that have been developed nor the many advances that have been made. An account of modern fission theory can be found in the recent book by Krappe and Pomorski [74]. In this Section, we shall first briefly describe the general conceptual framework for the most common theoretical treatments of nuclear fission dynamics. Subsequently, we shall turn to the more phenomenological modeling of fission, making contact with available data as far as possible.

11.3.1 *Fission dynamics*

As already recognized shortly after its discovery, the fission phenomenon can be understood as an evolution of the nuclear shape. The very concept of a nuclear *shape* is due to the basic character of the nucleonic interaction: it is attractive at long distances but very repulsive at short distances. Therefore, when nucleons are brought together (at low temperatures), there is an optimal spacing between neighbors or, equivalently, nuclear matter has a preferred density, the so-called saturation density. As a consequence, nuclei are *leptodermous* (thin-skinned), *i.e.* they have a fairly uniform interior, with a density near the saturation value, and are bounded by a relatively thin surface, having a thickness that reflects the (short) range of the nuclear force. Nuclei can therefore be depicted as (nearly) incompressible diffuse droplets of nuclear matter and, accordingly, the nuclear radius is proportional to the cube root of the nuclear mass number, $R_A = r_0 A^{1/3}$. This basic feature of nuclei is contrary to the character of atoms whose electron clouds grow steadily denser towards the center and whose sizes (*e.g.* their r.m.s. radii) do not increase steadily as one moves up through the Periodic Table.

Because of the leptodermous character of nuclear systems, it is natural, when seeking to develop a model of fission, to first decide which family of shapes to consider. Quite a number of different shape parameterizations have been suggested and employed. For an adequate description of nuclear fission, it is clearly necessary to consider at least three types of shape change: overall nuclear elongation (often measured in terms of the quadrupole moment of the matter distribution), the degree of indentation between the two emerging fragments (often described by the radius of the "neck" between the two parts), and the degree of reflection asymmetry. As it turns out, it may also be essential to allow individual deformations of the two pre-fragments, especially at lower excitations where shell effects play a role. On the other hand, the shapes may usually be regarded as having rotational symmetry around the axis connecting the centers of the two parts.

11.3.1.1 *Formal framework*

Let the multi-dimensional variable $\boldsymbol{q} = \{q_i\}$ specify a particular nuclear shape. The theoretical task is then to determine how $\boldsymbol{q}$ evolves from a value characteristic of the original nuclear compound nucleus towards two separated fragment nuclei. The commonly adopted approach consists in treating $\boldsymbol{q}$ as a collective variable subject to a dissipative coupling to the remainder of the system. Thus one must calculate not only the potential energy of a specified shape, $U(\boldsymbol{q})$, and the inertial-mass tensor associated with shape changes, $\boldsymbol{M}(\boldsymbol{q})$, but also the dissipation tensor characterizing the residual coupling, $\boldsymbol{\gamma}(\boldsymbol{q})$. The conservative part of the collective shape evolution is then described by the corresponding Lagrange function,

$$\mathcal{L}(\dot{\boldsymbol{q}}, \boldsymbol{q}) \;=\; \tfrac{1}{2} \sum_{ij} M_{ij}(\boldsymbol{q})\, \dot{q}_i\, \dot{q}_j - U(\boldsymbol{q}) \;, \tag{11.4}$$

and the associated collective momentum $\boldsymbol{p} = \{p_i\}$ has the components

$$p_i \;=\; \frac{\partial}{\partial \dot{q}_i} \mathcal{L}(\dot{\boldsymbol{q}}, \boldsymbol{q}) \;=\; \sum_j M_{ij}(\boldsymbol{q})\, \dot{q}_j \;. \tag{11.5}$$

Furthermore, the associated conservative driving force $\boldsymbol{F}^{\rm cons} = \{F_i^{\rm cons}\}$ has the components $F_i^{\rm cons}(\boldsymbol{q}, \dot{\boldsymbol{q}}) = \partial \mathcal{L}(\dot{\boldsymbol{q}}, \boldsymbol{q}) / \partial q_i$.

It was recognized by Bohr [10] several years before the discovery of fission that the time scale associated with the internal equilibration in a nucleus is relatively short, giving rise to the concept of a compound nucleus. Therefore it may be assumed that the internal rearrangements caused by a shape change occur sufficiently quickly for the internal degrees of freedom to remain close to equilibrium. Because the shape degrees of freedom are coupled to the internal system, their evolution will then resemble that of Brownian motion. The average effect of this dissipative coupling is a friction force $\boldsymbol{F}^{\rm fric} = \{F_i^{\rm fric}\}$ whose components are given by

$$F_i^{\rm fric}(\boldsymbol{q}, \dot{\boldsymbol{q}}) \;=\; -\frac{\partial}{\partial \dot{q}_i} \mathcal{F}(\dot{\boldsymbol{q}}, \boldsymbol{q}) \;=\; -\sum_j \gamma_{ij}(\boldsymbol{q})\, \dot{q}_j \;, \tag{11.6}$$

where the Rayleigh dissipation function,

$$\mathcal{F}(\dot{\boldsymbol{q}}, \boldsymbol{q}) \;=\; \tfrac{1}{2} \sum_{ij} \gamma_{ij}(\boldsymbol{q})\, \dot{q}_i\, \dot{q}_j \;=\; \tfrac{1}{2} \dot{Q}(\dot{\boldsymbol{q}}, \boldsymbol{q}) \;, \tag{11.7}$$

equals half the average rate of energy dissipation, *i.e.* the average rate at which energy is transferred from the shape motion to the internal degrees of freedom. The remainder of the dissipative force, $\boldsymbol{F}^{\rm ran} = \boldsymbol{F}^{\rm diss} - \boldsymbol{F}^{\rm fric}$, is usually assumed to be random in character and have a Markovian time dependence,

$$\langle \boldsymbol{F}_i^{\rm ran}(t) \boldsymbol{F}_j^{\rm ran}(t') \rangle \;=\; 2T\, \gamma_{ij}\, \delta(t - t') \;, \tag{11.8}$$

where T is the nuclear temperature. It should be noted that it is the *same* tensor, $\boldsymbol{\gamma} = \{\gamma_{ij}\}$, that enters in both (11.7) and (11.8), in accordance with the fluctuation-dissipation theorem [75, 76].

The equation of motion for the time evolution of the nuclear shape is then obtained by equating the rate of momentum change with the forces acting,

$$\frac{\partial}{\partial t}\boldsymbol{p} \;=\; \boldsymbol{F}^{\rm cons}(\dot{\boldsymbol{q}},\boldsymbol{q}) \;+\boldsymbol{F}^{\rm fric}(\dot{\boldsymbol{q}},\boldsymbol{q}) \;+\boldsymbol{F}^{\rm ran}(\dot{\boldsymbol{q}},\boldsymbol{q}) \;. \tag{11.9}$$

It is often referred to as the *Langevin* equation because of the presence of the random part of the dissipative force. It is thus a stochastic equation and it is most easily solved by direct simulation, *i.e.* starting from the specified initial state (or ensemble of initial states), one generates a (sufficiently large) sample of individual evolution histories by using suitable random numbers for the stochastic force.

11.3.1.2 *Potential*

The most basic quantity needed is the multi-dimensional surface describing the potential energy of the fissioning nucleus as a function of the nuclear shape. While the overall, large-scale, features of the potential-energy landscape can be understood on the basis of the liquid-drop model, its local value may deviate significantly from the smooth average due to the shell structure of the particular shape considered. Therefore, the potential energy is usually calculated by means of a hybrid approach, the so-called macroscopic-microscopic method, by which the smooth average is obtained from a suitable macroscopic model, while the local fluctuations are obtained microscopically by solving the Schrödinger equations for the individual nucleons in the associated deformed effective field and then extracting the pairing and shell corrections, $U(\text{shape}) = U_{\rm macro}(\text{shape}) + U_{\rm micro}(\text{shape})$.

A thorough discussion of this approach was given in Ref. [77]. That work employed a two-dimensional shape parameterization, describing overall elongation and reflection asymmetry, but richer shape families are required for realistic treatments of fission. The so far most detailed shape family had been introduced previously by Ray Nix [78]; its shape are formed by three smoothly joined portions of quadratic surfaces and thus encompasses five distinct shape degrees of freedom: elongation, indentation, asymmetry, and independent distortions of the two pre-fragments. For this shape family (and others as well), using the finite-range liquid-drop model for the macroscopic energy, BCS theory for the paring correction, and the Strutinsky procedure for the shell correction, Peter Möller and collaborators have calculated the potential energy for a essentially all fissionable nuclei (more than five thousand), on a five-dimensional lattice containing over five million shapes [79, 80].

Knowledge of the potential energy landscape enables one to anticipate how the shape may evolve towards fission. The locations of isomeric minima and the saddle points between minima are particularly important. Thus, by surveying the landscape beyond the saddle, it is usually possible to predict the most probable mass split and, in some cases, notably in the fermium region, the occurrence of bimodal fission can be traced to the presence of different possible fission paths.

11.3.1.3 *Inertia*

The inertial mass tensor for the nuclear shape motion is still not quantitatively understood, even though much progress has been made. The most common is therefore to simply assume that the flow is incompressible and irrotational. While this is generally expected to become reasonably accurate at sufficiently high excitations where the shell effects have subsided, it is less accurate at more moderate excitations where the elements of the inertial mass tensor $\boldsymbol{M}(\boldsymbol{q})$ exhibit large variations as the shape is changed and also tend to be larger than those for the corresponding incompressible-irrotational flow. Nevertheless, that simple approach may be a reasonable starting point because recent research suggests that the outcome of the fission dynamics may not be critically dependent on the details of the inertia (see Sect. 11.3.1.6).

Linear response theory provides a general and powerful formal framework for calculating both the inertias and the dissipation associated with the nuclear collective motion and a thorough discussion of the approach can be found in the recent book by Helmut Hofmann [81].

11.3.1.4 *Dissipation*

The magnitude and structure of the shape dissipation tensor $\boldsymbol{\gamma}(\boldsymbol{\chi})$ is still a central issue in the field. Early calculations employed a fluid-dynamical viscosity with an adjustable strength, but nowadays the shape dissipation tensor is most often based on the so-called one-body dissipation mechanism which considers the dissipative interaction of individual nucleons with the evolving effective one-body mean field [53]. It takes a particularly simple form for an irregular mono-nuclear shape, such as a nucleus in the region of the fission saddle point,

$$\dot{Q}_{\rm wall} \;=\; m_n \rho \bar{v} \oint u_n^2 \, d\sigma \;. \tag{11.10}$$

The integral is over the nuclear surface and u_n denotes the local surface velocity normal to the surface. The overall strength is given by the product of the mass density of the nucleons, ρ, and their mean speed, $\bar{v} \approx \frac{3}{4} v_F$. The resulting dissipation is fairly strong (and nearly energy independent) and causes the shape motion to become overdamped, rendering the inertial mass tensor $\boldsymbol{M}(\boldsymbol{\chi})$ less crucial.

As the nucleus approaches scission, it attains a binary character, with the two parts being in (mostly radial) relative motion. The above *wall* formula (11.10) must then be augmented by the *window* formula which yields the energy dissipation caused by the transfer of nucleons between the two moving binary partners,

$$\dot{Q}_{\rm window} \;=\; \tfrac{1}{4} m_n \rho \bar{v} \, \pi c^2 (2u_\parallel^2 + u_\perp^2) \;. \tag{11.11}$$

Here $u_\parallel$ is the relative radial velocity of the two pre-fragments, $u_\perp$ is the transverse velocity component, and c is the radius of the neck connecting the two parts.

The one-body dissipation produces fission paths that differ in essential ways from those resulting from a viscosity. Importantly, one-body dissipation causes the

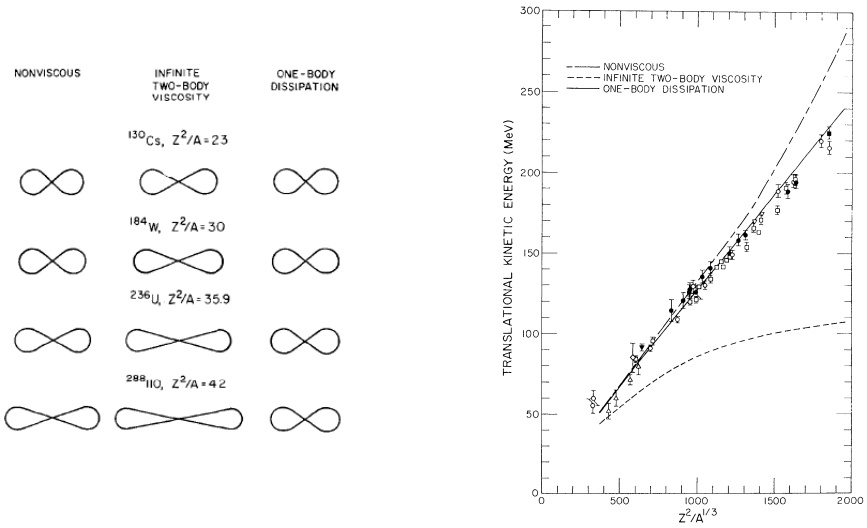

Fig. 11.17 *Left:* For fission of four nuclei is shown the scission shapes obtained with either non-viscous flow (left column), infinite two-body viscosity (center column), or wall-plus-window one-body dissipation with standard strength (right column). *Right:* Total fission fragment kinetic energy as measured or calculated with the three types of dissipation. Adapted from Ref. [53].

scission shapes to be rather compact and the relative motion rather slow, whereas a viscosity yields rather stretched scission configurations for which the two parts are already in appreciable relative motion. This is illustrated in Fig. 11.17 (*left*).

Early support for the dominance of the one-body dissipation mechanism in fission dynamics was provided by the dependence of TKE on Z^2/A, where Z and A denote the charge and mass numbers of the fissioning nucleus, see Fig. 11.17 (*right*). Generally TKE increases with Z^2/A due to the growing dominance of the Coulomb energy. Calculations (ignoring the random force) without any dissipation at all yield TKE values that are too large, whereas those using an infinite viscosity underpredict TKE; it is possible to adjust the viscosity strength so that TKE(Z^2/A) is reasonably reproduced. Remarkably, calculations using the wall-plus-window one-body dissipation readily reproduce this function without the need for any adjustment. Furthermore, the experimental TKE values are not very dependent on the initial nuclear excitation energy, indicating that the dissipation is only weakly dependent on temperature, a general characteristic of the one-body mechanism. Further studies were made in Ref. [82].

Because of this success and further supportive evidence from damped nuclear reactions [83, 84], one-body dissipation has found widespread use in dynamical fission calculations. However, both theoretical considerations and further comparisons with data suggest that the overall strength of the one-body dissipation tensor should be reduced by about a factor of four (which will not change the results in Fig. 11.17).

11.3.1.5 *Langevin simulations*

The general framework described above has found extensive use for the description of heavy-ion fusion, damped nuclear reactions, and heavy-ion induced fission and numerous studies have been made of the multi-dimensional fission dynamics.

In a broad line of work, Fröbrich and Gontchar [28] developed a Langevin description of fusion, deep-inelastic collision, and heavy-ion-induced fission from an idealized schematic model. With the aim of reproducing the experimental data, the potential and the transport coefficients for fusion and deep-inelastic collisions were taken from a phenomenological surface friction model, whereas for heavy-ion induced fission they invoked statistical considerations. In this manner they obtained a universal reproduction of the data for a multitude of observables and they also made comparison with related work by others.

Langevin studies of fission dynamics at lower energies, where shell and pairing effects are present, were carried out with the a two-dimensional shape family of Ref. [77], but coupling the shape evolution to the pre-fission neutron evaporation and also taking account of angular momentum [85, 86]. Although quite successful for the region of symmetric fission at high excitation, comparison with experimental data suggested that there was a need to extend the dimensionality of the shape family when going to lower energy. Furthermore, it was found that the fragment mass distribution could provide useful information about the dissipation.

In a more recent effort, Langevin calculations of the mass, energy, charge, and angular distributions of fragments formed by fission of excited nuclei have been done with a three-dimensional shape family for a wide range of fissilities and nuclear excitations [87]. A temperature-dependent finite-range liquid-drop model, taking into account the diffuse nuclear surface, was used in a consistent way to calculate the potential energy and the level-density parameter. The dissipation of the collective motion was described by a modified one-body mechanism (see below) with a reduction of the wall contribution. The evaporation of light pre-scission particles was taken into account on the basis of a statistical model combined with the Langevin dynamics. The multi-dimensional Langevin calculations yielded a satisfactory reproduction of the observed distributions of fission fragments with respect to mass and kinetic energy as well as the pre-fission neutron multiplicity.

Very recently, in a four-dimensional space in which the three-dimensional shape family of Ref. [87] was extended to four dimensions by considering also the nuclear orientation, a Langevin study was made of various oxygen-induced fission reactions, including also dynamical neutron evaporation. This yielded reasonable agreement with the observed evaporation residue cross sections, fission-fragment mass-energy distributions, pre-scission neutron multiplicities, and fission-fragment angular anisotropies [88].

11.3.1.6 *Brownian shape dynamics*

Because the dissipation associated with the nuclear shape dynamics is relatively strong, the shape changes will be relatively slow and hence it might be expected that it would be reasonable, at least as a starting point, to ignore inertial forces altogether (by putting the inertias to zero). The equation of motion then simplifies,

$$0 \;=\; -\partial U(\boldsymbol{q})/\partial \boldsymbol{q} \;-\boldsymbol{\gamma}(\boldsymbol{q})\cdot\dot{\boldsymbol{q}} + \boldsymbol{F}^{\rm ran}(\dot{\boldsymbol{q}},\boldsymbol{q},t)\;. \tag{11.12}$$

This is the Smoluchowski limit describing Brownian motion. In nuclear fission, the N-dimensional nuclear shape represents the test body and the residual system forms the statistical reservoir to which it is coupled. Thus the scenario is more complicated than the familiar Brownian motion: it occurs in N dimensions (the dimensionality of the shape parameter $\boldsymbol{q}$), the medium is anisotropic ($\boldsymbol{\gamma}$ is not diagonal) and non-uniform ($\boldsymbol{\gamma}$ depends on $\boldsymbol{q}$), and the body is situated in an external potential, $U(\boldsymbol{q})$.

This idealization was recently explored [90] with the five-dimensional shape family for which the potential has been tabulated on a Cartesian lattice [80]. Further simplification emerges if the dissipation tensor $\boldsymbol{\gamma}$ is isotropic, *i.e.* proportional to the unit tensor for any shape, $\boldsymbol{\gamma}(\boldsymbol{q}) = \gamma(\boldsymbol{q})\boldsymbol{I}$, because the shape evolution can then be simulated by a Metropolis walk on the potential energy lattice [89]. Figure 11.18 shows fragment charge yields obtained in this manner compared with the corresponding experimental data. The agreement is remarkable and at first sight somewhat puzzling. However, further studies [90] suggest that the charge yield is rather insensitive to anisotropies in $\boldsymbol{\gamma}$, presumably because a large degree of equilibration takes place in the course of the strongly damped evolution. Thus, even though the dissipation tensor is nowhere near isotropic, the idealization may nevertheless be quantitatively useful and it is currently being utilized to make extensive survey calculations of fragment yields in various regions of the nuclear chart.

These studies [89, 90] have already brought out a number of instructive features. Probably most importantly, it appears that the potential energy surface is a crucial determinant for the outcome of the fission process. Thus it was demonstrated that a correspondingly good reproduction of the yields could not be achieved with a shape family of lower dimensionality. Furthermore, it was possible to dismiss the long-held belief that the character of the fragment yield, whether symmetric or asymmetric, was determined by the character of the saddle shape (^{222}Th has an asymmetric saddle shape but a symmetric fission yield), suggesting that the shape evolution from saddle to scission is non-trivial. This conclusion was further supported by comparisons with yield expectations based on the relative statistical weight of scission configurations, among the earliest models proposed for fission yields [91, 92]. Such models were found to exhibit strong sensitivity to the definition of the scission shapes whose weights were compared, in contradistinction to the outcomes of dynamical calculations which tend to be very robust against when the calculation is stopped because by then the mass split is well determined. An extensive review of nuclear scission was given by Brosa *et al.* [93].

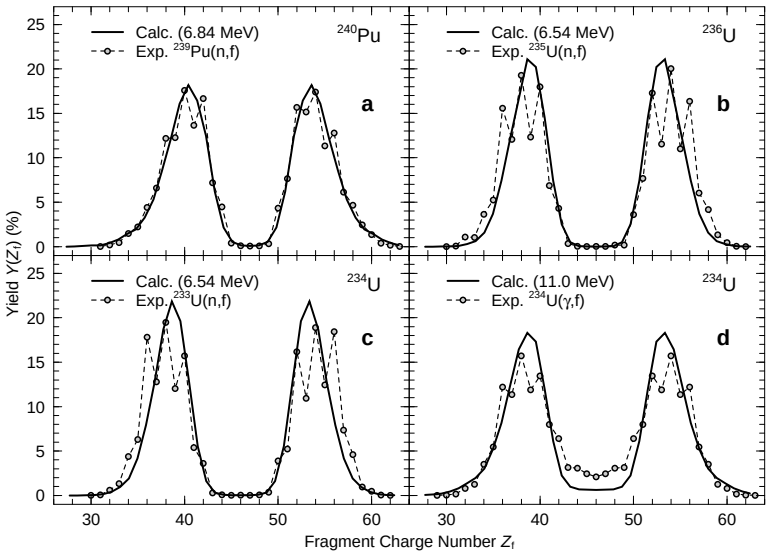

Fig. 11.18 Calculated and measured charge yields for fission of ^{240}Pu and ^{236,234}U; the data in (a)-(c) are for ($n_{\rm th}$,f), while those in (d) are for (γ,f) reactions leading to $E^* \approx 8 - 14\,$MeV (the corresponding calculation was made for $E^* = 11\,$MeV). [From Ref. [89].]

11.3.1.7 *Microscopic fission dynamics*

The transport treatments discussed above have proven to provide both practical and powerful means for obtaining quantitatively useful results and for gaining physical insight into the fission phenomenon. However, from a theoretical perspective, it is desirable to ultimately be able to describe the process within a self-consistent quantum-mechanical microscopic framework. Efforts towards this goal have been underway for decades and it is beyond the present scope to attempt a review here.

The most advanced microscopic studies of fission employ the constrained Hartree-Fock-Bogoliubov method with an effective finite-range density-dependent nucleon-nucleon interaction. On this basis, purely static studies have yielded very instructive results for a number of actinide isotopes, see in particular Refs. [94, 95].

Within this framework, invoking the time-dependent generator coordinate method, making use of the Gaussian overlap approximation, and relying on the adiabatic assumption (that the collective dynamics decouples from the intrinsic system), Goutte and collaborators [96] have derived Schrödinger equations of motion for the collective amplitudes and applied this dynamical model to fission of ^{238}U. Analyses of the resulting evolution and comparison of the extracted fragment mass and energy distributions are encouraging and suggest that further improvements of the model would be worthwhile. These studies, whether static or dynamic, have so far included only quadrupole and octupole constraints and the authors draw particular attention to the possibility that more shape flexibility may be needed.

11.3.2 *Modern modeling of fission observables*

In the preceding section we have discussed the theoretical treatment of the shape evolution associated with nuclear fission. Because the fission process itself is accompanied by a variety of other processes, most notably the emission of several neutrons, there is a need for developing models that encompass the entire phenomenon. Such modeling is particularly needed for generating the data evaluations used by application codes that require accurate knowledge of the prompt fission neutron spectrum for different fissile isotopes over a wide range of incident neutron energies. Since the early 1980's, most evaluations of fission data have employed a 'standard model' of prompt fission neutron emission which we describe briefly below. Subsequently, we will discuss current efforts to go beyond such average treatments by to Monte Carlo techniques.

11.3.2.1 *Traditional models*

The dominant method of calculating the prompt fission neutron spectra, of critical importance for nuclear databases used in simulating fission for stockpile stewardship and reactor studies, has been the 'Los Alamos model' introduced by Madland and Nix [97]. This model was developed to improve upon earlier calculations using Maxwell distributions with parameters adjusted to data. That approach had several shortcomings, including the fact that the neutron spectrum, even under idealized circumstances, is not of Maxwellian form; even if it were, it would be distorted by the motion of the emitting nucleus; and the spectrum should soften due to the cooling of the fragment as more neutrons are emitted.

The Madland-Nix approach uses the Weisskopf-Ewing spectral shape, $dN_n/dE \sim E \exp(-E/T_{\max})$, where E is the relative kinetic energy of the emitted neutron and $T_{\max}$ is the maximum temperature of the daughter nucleus, corresponding to $E = 0$. Relative to the thermal (Maxwellian) spectrum, the Weisskopf-Ewing spectrum contains an additional factor $\sim \sqrt{E}$, as elementary considerations would suggest (the faster a neutron moves inside the nucleus, the sooner it is emitted, skewing the thermal spectrum by a velocity factor). It is easy to see that the mean neutron kinetic energy is $\langle E \rangle = 2T$.

Once the energy of the neutron is known, the excitation energy of the daughter nucleus follows by conservation and the nuclear temperature T is then obtained with the simple Fermi gas model, $E^* = aT^2$, where the level density parameter is taken as $a = A/e_0$ with $e_0 \approx 8 - 10$ MeV. Because the actual neutron energy E is stochastic, so is the resulting excitation of the daughter nucleus. As a particular simplification, the Madland-Nix model assumes that the corresponding T distribution, $P(T)$, is triangular, because the average neutron spectrum can then be obtained on an analytical form,

$$\left(\frac{dN_{\rm n}}{dE}\right)_{\rm ave} = \int_0^{T_{\max}} \frac{dN_{\rm n}}{dE}\, P(T)\, dT = \frac{2E}{T_{\max}^2} \int_0^{T_{\max}} {\rm e}^{-E/T}\, \frac{dT}{T}\ . \qquad (11.13)$$

The overall average neutron energy is then $\langle E \rangle = \frac{4}{3} T_{\max}$. If the fragment moves with its average kinetic energy, $E_{\rm f} = (1 - A_{\rm f}/A)\overline{\rm TKE}$, the average prompt fission neutron spectrum in the laboratory frame can also be obtained analytically.

In the original work by Madland and Nix [97], the light and heavy fragments were assumed to be the most probable ones, while a local average value, $\langle S_n \rangle$, was used for the neutron separation energy. Furthermore, the average total initial fragment excitation energy, $\langle E^*_{LH} \rangle$, was obtained by subtracting the measured average total fragment kinetic energy, $\overline{\rm TKE}$, from the appropriate Q value, Q_{LH}. The average neutron multiplicity for a given fragment was then obtained as

$$\overline{\nu} \;=\; \frac{\langle E^*_{LH} \rangle - \langle E_\gamma \rangle}{\langle S_n \rangle + \langle E \rangle} \;, \tag{11.14}$$

where $\langle E_\gamma \rangle$ is the average energy radiated away by photons. Multichance fission can be approximated using a model of $n^{\rm th}$-chance fission cross sections relative to the total fission cross section and adjusting the neutron multiplicity by the ratio of these cross sections.

The resulting average spectra, based on these simplifying assumptions, are completely smooth. No information about the initial fragment identities or kinetic energies are available beyond the average. Furthermore, the spectra are independent of the neutron multiplicity so that their shapes are identical no matter how many neutrons are emitted.

The Madland-Nix model [97] has been very useful and a number of variants have been introduced with further refinements (see, for example, Ref. [98]). It is still being used as the basis for spectral evaluations and most simulations of prompt fission neutron emission.

11.3.2.2 *Monte Carlo based methods*

While the Madland-Nix model [97] has been used very successfully for both reproducing the measured prompt fission neutron spectra where measurements exist and for making predictions of the spectra where no data are available, see Figs. 11.12 and 11.13, it cannot be used for calculating other quantities without considerably expanding the number of parameters [98]. To gain more physics insights into the fission process, especially near scission, it is necessary to address more exclusive data, such as the neutron multiplicity as a function of fragment mass, shown in Fig. 11.4, and the neutron multiplicity distribution, shown in Fig. 11.10. To go beyond average models, it is most convenient to employ Monte Carlo methods to simulate the individual fission events, thus obtaining a sample of events from which both fluctuations and correlations may be subsequently extracted, much as one would analyze an ideal experiment. These approaches will be briefly described in the following.

Monte Carlo methods are particularly useful when used to simulate the entire fission process and produce large samples of complete fission events, conserving

energy and momentum at each step while retaining full kinematic information on the emerging fission products and the emitted neutrons and photons. With this information it is straightforward to extract the behavior of any quantity of interest, including correlations between different quantities.

Several groups that have been developing Monte Carlo approaches since 2005. Lemaire *et al.* made the first Monte Carlo calculations of evaporation of prompt neutrons [99] and photons [72] from ^{235}U(n,f) and ^{252}Cf(sf). Some of the same authors are now pursuing a more refined approach with first results on ^{239}Pu(n,f) using the `FFD` code having recently appeared [100]. Shortly after the Lemaire papers, Randrup and Vogt introduced the Monte Carlo model `FREYA` (*Fission Reaction Event Yield Algorithm*) [30, 32, 101] which produces samples of complete events. It has been employed to develop evaluations for ^{239}Pu(n,f) and ^{235}U(n,f), for incident neutron energies up to 20 MeV [101, 30] as well as to study correlations in neutron-induced and spontaneous fission [32, 73]. It is now being used to study photon observables in more detail in these same isotopes [102]. Two other recent Monte Carlo models recently introduced are `FIFRELIN` (*Fission Fragment Evaporation Leading to an Investigation of Nuclear Data*) by Litaize and Serot [103] and `GEF` by Schmidt and Jurado [104] which incorporates a model of fission fragment yields based on an extensive set of measured yields.

All the models require some amount of experimental or theoretical input. Like all Monte Carlo treatments, any extrapolation of parameters or calculations outside the range of inputs may lead to inaccurate predictions. Thus more and better data, as well as improved theoretical input, are necessary to make further progress with Monte Carlo approaches and improve predictive capability.

In the remainder of this section, we first discuss features common to all approaches. We then compare some of the current model results. Finally, we show some correlation observables that could potentially be measured and might prove useful in applications looking at small amounts of fissile material in particular.

11.3.2.3 *Fragment properties*

Sections 11.2.2.1 and 11.2.2.2 describe some of the characteristics of the fragment yields and total kinetic energies immediately after scission. The ideal Monte Carlo input data would include the fragment yields as a function of mass, charge, and kinetic energy, $Y(A, Z, \mathrm{TKE})$. In practice, there is typically a measurement of only one of these quantities, averaged over the other two. Once the fragment charges and masses are identified, the total energy in the fission event, the Q value, is obtained. This energy is divided between the total kinetic energy and the total excitation energy of the fragments. If the TKE is sampled, the excitation energy, TXE, is known from energy conservation.

`FREYA` makes use of measured mass yields, $Y(A)$, and total kinetic energies. To reach incident neutron energies of up to 20 MeV, the energy dependence of the yields was parameterized from data, making certain model assumptions and taking

multichance fission into account [30]. The shape of the total kinetic energy has been assumed to remain approximately constant as a function of incident energy and an adjustable energy shift, dTKE, was introduced to retain agreement with the total average neutron multiplicity, $\overline{\nu}$. `FREYA` is the only Monte Carlo so far to include multichance fission and pre-equilibrium neutron emission.

Once the fragment mass has been selected, the charge of the fragment, Z_f, is sampled from a Gaussian distribution [38], $P_{A_f}(Z_f) \sim \exp[-(Z_f - \overline{Z}_f(A_f))^2/2\sigma_Z^2]$. The centroid is determined by requiring that the fragments have, on average, the same charge-to-mass ratio as the fissioning nucleus, $\bar{Z}_f(A_f) = A_f Z_0/A_0$, while the variance is given by $\sigma_Z^2 = (\sigma_Z^0)^2 + \frac{1}{12}$, with σ_Z^0 having been determined experimentally, [38]. The charge of the complementary fragment follows from $Z_L + Z_H = Z_c$.

`FIFRELIN` has only published results so far for spontaneous fission of ^{252}Cf(sf). It makes use of the measured fragment yields, $Y(A)$, and a mass-dependent Gaussian function characterized by a measured mean kinetic energy and dispersion [103],

$$Y[\mathrm{KE}(A)] \;\sim\; \exp\left\{ -\left[\mathrm{KE} - \langle \mathrm{KE}\rangle(A)\right]^2 / 2\sigma_{\mathrm{KE}}(A)^2 \right\} . \tag{11.15}$$

It uses the same charge selection procedure as `FREYA`.

The latest results by Talou *et al.* on ^{239}Pu(n,f) are only for thermal neutrons so far [100]. They make a least-squares fit to experimental mass yields, $Y(A)$, as well as data on the total kinetic energy as a function of heavy fragment mass, A_H. They also use the measured width of TKE(A_H) to obtain a Gaussian similar to Eq. (11.15) above but with KE(A) replaced by TKE(A_H). They assume that the mean of the charge density distribution is adjusted by a deviation ΔZ, and an odd-even factor, $F(A)$, so that

$$Y(Z|A) \;\sim\; F(A)\left[\mathrm{erf}(V_+) - \mathrm{erf}(V_-)\right] , \tag{11.16}$$

where $V_\pm = (Z - \bar{Z} \pm 0.5)/(\sqrt{2}\sigma_Z)$.

When the mass and charge of each fragment have been selected, the associated fission Q value follows. After scission has occurred, the two fragments are being accelerated in their mutual Coulomb field as their shapes relax to their respective equilibrium forms. In addition to the resulting relative translational motion, the emerging fragments generally carry angular momentum, $\boldsymbol{S}_L$ and $\boldsymbol{S}_H$, so the energy available for statistical excitation of the fragments is

$$E_L^* + E_H^* \;=\; Q_{LH} - \mathrm{TKE} - E_L^{\mathrm{rot}} - E_H^{\mathrm{rot}} . \tag{11.17}$$

The nuclear rotational is treated in a rather schematic manner, the energy being $E^{\mathrm{rot}} = S^2/2\mathcal{I}$, where the moment of inertia is typically half the rigid value, $\mathcal{I} \approx \frac{1}{2}\mathcal{I}_{\mathrm{rigid}} = \frac{1}{5} m_N A R^2$, where $R = r_0 A^{1/3}$ is the fragment radius.

Employing a "spin temperature" parameter T_S, `FREYA` first samples the angular momenta of the two fragments and then subtracts the associated rotational energies as well as the experimentally measured average kinetic energy, $\overline{\mathrm{TKE}}$ (plus a small common amount adjusted to ensure correct reproduction of the overall average neutron multiplicity), to obtain the average total statistical excitation, which

is subsequently divided between the two fragments by equipartition. A small redistribution is then made in favor of the light fragment to emulate its typically larger scission distortion. Subsequently, associated energy fluctuations, δE_f^*, are sampled statistically, by use of a Fermi gas, and the total fragment kinetic energy is adjusted correspondingly, $\mathrm{TKE} = \overline{\mathrm{TKE}} - \delta E_L^* - \delta E_H^*$. This procedure will be discussed further in Sect. 11.3.2.5.

The `GEF` code [104] employs a model of the potential energy surface of the fissioning nucleus near scission to calculate the fragment yields as a function of charge and mass. Using this method, they obtain the total intrinsic excitation energy E_{int}^* at scission from the initial energy of the fissioning nucleus, E_{CN}^*; the height of the fission barrier, E_{B}; and the energy released on the way from saddle to scission dissipated into excitation energy, E_{diss} [105], $E_{\mathrm{int}}^* = E_{\mathrm{CN}}^* - E_{\mathrm{B}} + E_{\mathrm{diss}}$. For example, in neutron-induced fission, the initial energy, E_{CN}^*, is the sum of the incident neutron energy and the neutron separation energy. In this model then, the excitation energy is obtained directly, obviating the need for the total fragment kinetic energy used in all other Monte Carlo treatments.

11.3.2.4 *Fragment de-excitation*

Usually both fully accelerated fission fragments are excited sufficiently to permit the emission of one or more neutrons. After neutron emission is no longer energetically possible, the remaining excitation energy is radiated by photons. Initially photon emission is also statistical. However, when the excitation energy reaches the yrast line, photon emission is along this line, passing through discrete levels until the fragment is no longer excited. We note that, as of yet, no Monte Carlo code treats the competition between neutron and photon emission realistically near the limit of neutron evaporation, the sum of the neutron separation energy, S_n, and the collective rotational energy of the fission fragment, E_f^{rot}.

Neutron evaporation. Neutron emission is treated by iterating a simple neutron evaporation procedure for each of the two fragments separately. At each step in the evaporation chain, the excited mother nucleus ${}^{A_i}Z_i$ has a total mass equal to its ground-state mass plus its excitation energy, $M_i^* = M_i^{\mathrm{gs}} + E_i^*$. The Q-value for neutron emission from the fragment is then $Q_n = M_i^* - M_f - m_n$, where M_f is the ground-state mass of the daughter nucleus and m_n is the mass of the neutron. (For neutron emission we have $A_f = A_i - 1$ and $Z_f = Z_i$.) The Q-value is equal to the maximum possible excitation energy of the daughter nucleus, achieved if the final relative kinetic energy vanishes. The temperature in the daughter fragment is then maximized at T_f^{max}.

Thus, once Q_n is known, the kinetic energy of the evaporated neutron may be sampled. Most models assume that the neutrons are emitted isotropically from the mother nucleus with the spectral shape taken from the Weisskopf-Ewing distribution

[106] used already by Madland and Nix [97],

$$f_n(E) \equiv \frac{1}{N_n}\frac{dN_n}{dE} \sim E\,\mathrm{e}^{-E/T_f^{\max}} , \tag{11.18}$$

which can be sampled efficiently [32]. It is assumed that the fragment retains all of its angular momentum. The daughter excitation is then given by $E_f^* = Q_n - E$ and its total mass is thus $M_f^* = M_f^{\rm gs} + E_f^*$. The magnitude of the momenta of the excited daughter and the emitted neutron can then be determined [32]. Sampling the direction of their relative motion isotropically, one may thus obtain the momenta of the neutron and the daughter fragment; these are subsequently boosted into the overall reference frame by the appropriate Lorentz transformations.

This procedure is repeated until no further neutron emission is energetically possible, which occurs when $E_f^* < S_n + E_f^{\rm rot}$, where S_n is the neutron separation energy in the prospective daughter nucleus, $S_n = M(^A Z) - M(^{A-1}Z) - m_n$. no d!

Photon radiation. After the neutron evaporation has ceased, the excited product nucleus may de-excite by sequential photon emission. This process is treated in a manner analogous to neutron evaporation, *i.e.* as the statistical emission of massless particles until the fragment excitation energy reaches the yrast energy for that fragment.

There are two important technical differences relative to the treatment of neutron emission. There is no separation energy for photons and, because they are massless, there is no obvious end to the photon emission chain (which necessitates the introduction of an infrared cut-off). Whereas the neutrons may be treated by nonrelativistic kinematics, the photons are ultrarelativistic. As a consequence, there is an extra energy factor in the phase-space Jacobian,

$$f_\gamma(E) \equiv \frac{1}{N_\gamma}\frac{dN_\gamma}{dE} \sim E^2\,\mathrm{e}^{-E/T_f^{\max}} . \tag{11.19}$$

The photons are assumed to be emitted isotropically and their energy can be sampled very quickly from the above photon energy spectrum [32]. This procedure is repeated until the available energy reaches the yrast line, at which point the photons are emitted from the yrast bands with discrete energies corresponding to a reduction of the angular momentum by two units. Thus a number of kinematically fully-characterized photons are emitted from each of the two product nuclei.

11.3.2.5 *Fragment temperature distributions*

Finally, we discuss the resulting temperature distributions in the fragments after neutron evaporation. At each stage of the neutron evaporation chain, the excitation of the daughter nucleus is the difference between the evaporation Q-value and the kinetic energy of the evaporated neutron, E. Consequently, the spectral distribution of E will cause T to have a corresponding distribution, $P(T)$. Even at the first evaporation stage, the T distribution will be non-trivial because the initial excitation of the emitting fragment has itself a distribution, as described above.

The temperature distributions in the daughter, granddaughter, and great granddaughter nuclei are shown in Fig. 11.19 as obtained with FREYA for six particularly interesting cases of either spontaneous or thermal-neutron induced fission. The temperatures in the daughter nuclei ($\nu = 1$) are fairly well peaked at around 0.5-0.8 MeV; the larger contributions come from the light fragment which tends to be hotter than its heavy partner. The temperature distributions in the granddaughter nuclei ($\nu = 2$) are considerably broader and peak at lower energies, and they decrease monotonically for the great-granddaughters ($\nu = 3$).

For spontaneous fission of ^{240}Pu and ^{238}U, where the average total neutron multiplicity is only $\overline{\nu} \approx 2.15$ and 2.0, respectively, each fragment is likely to emit only a single neutron so that either fragment is relatively unlikely to emit three neutrons, so $P_3(T)$ is quite small. The induced fission processes ^{239}Pu($n_{\rm th}$,f) and ^{235}U($n_{\rm th}$,f) lead to higher daughter temperatures than ^{240}Pu(sf) and ^{238}U(sf) and they also yield larger multiplicities. Thus $\overline{\nu} \approx 2.88$ for ^{239}Pu($n_{\rm th}$,f) relative to 2.15 for ^{240}Pu(sf), and $\overline{\nu} \approx 2.47$ for ^{235}U($n_{\rm th}$,f) relative to 2.0 for ^{238}U(sf). Spontaneous fission of ^{244}Cm and ^{252}Cf also results in higher daughter temperatures. Indeed, the temperature distributions are similar for ^{244}Cm(sf) and ^{239}Pu(n,f), as are the average neutron multiplicities (2.72 and 2.88, respectively). For ^{252}Cf(sf) the daughter temperature peaks at a higher value than in all the other cases considered and the tail extends further as well. In addition, the distribution of the temperature in the granddaughter fragments has a distinct peak around $T \approx 0.6$ MeV, not surprising since $\overline{\nu} \approx 3.75$ for ^{252}Cf(sf).

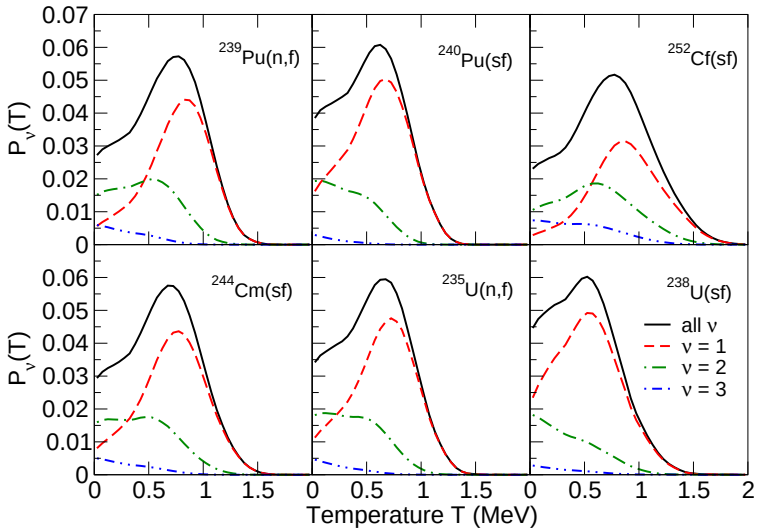

Fig. 11.19 The distribution of the temperature in the daughter nucleus, $P_\nu(T)$, after ν neutrons have been evaporated from a primary fragment, calculated with FREYA and normalized such that $\sum_\nu P_\nu(T) = P_{{\rm all}\,\nu}(T)$, for six cases of either spontaneous or thermal-neutron induced fission.

In the treatment by Madland and Nix [97] a convenient analytical expression was obtained by assuming that the overall distribution of the daughter temperature, $P_{\mathrm{all}\,\nu}(T)$, has a triangular shape. The results in Fig. 11.19 demonstrate that such an assumption is unrealistic, even for just $\nu = 1$.

11.3.3 *Model results*

We now compare neutron results from the available fission Monte Carlo calculations. Two of the most important quantities for the applied physics community are the average neutron multiplicity, $\overline{\nu}$, known to rather high precision, and the average neutron spectrum. The applications particularly focus on ^{239}Pu(n,f) and ^{235}U(n,f), along with ^{252}Cf(sf) which is a well-measured calibrator. Thus much of the available data are on these major isotopes. This section will focus on model results on ^{239}Pu(n,f) and ^{252}Cf(sf). For results on other actinides, see *e.g.* Refs. [73, 104].

We first compare results for the neutron multiplicity as a function of fragment mass, $\nu(A)$, for ^{252}Cf(sf) and ^{239}Pu(n,f) with $E_n = 0.5$ MeV. We then show the neutron multiplicity distribution, $P(\nu)$, for ^{239}Pu(n,f). We present the results for one of the model calculations for ^{239}Pu(n,f) relative to a Maxwellian and, finally, show a result for the residual energy left over for photon emission in ^{252}Cf(sf).

The dependence of the average neutron multiplicity on the fragment mass number A, is very sensitive to the division of the excitation energy which is governed by the parameter x in `FREYA` [73] and in the temperature ratio, R_T in `FFD` [100] and `FIFRELIN` [103]. As shown in Figs. 11.20 and 11.21, all the models reproduce the characteristic 'sawtooth' behavior.

There are numerous measurements of $\overline{\nu}(A)$ for ^{252}Cf(sf), shown in Fig. 11.20. Each of the model calculations compares to different data sets. However, all the data are remarkably similar. While there are differences near the peak of the sawtooth, these are generally rather small. Only the Wahl systematics, based on data taken before 1988 [108], plotted as the open circles in the bottom panel of Fig. 11.20 exhibit a different shape. The `FIFRELIN` results (top left) are shown for $R_T = 1.25$ and two different assumptions of the momenta of inertia of the rotating fragments. Both calculations give quite similar values of $\nu(A)$ and also agree rather well with the `FREYA` result with $x = 1.3$ on the top right panel of the figure. Both calculations show a higher and broader shoulder for the light fragment than the data and also have a less pronounced slope of $\nu(A)$ for $A > 145$. Changing x or R_T does not change the slopes of $\overline{\nu}(A)$, only the relative magnitudes. To better describe $\overline{\nu}(A)$, it would be necessary to fix $x(A)$ or $R_T(A)$ rather than employing just a single-valued parameter for x. Indeed, when `FIFRELIN` is run with an A dependent value of R_T, the agreement is improved. The `FREYA` result also includes the variance on $\nu(A)$, in addition to the average result. The `GEF` result follows the data of Ref. [109] rather closely with an almost linear slope of $\nu(A)$ for the light fragment, with no characteristic shoulder for the light fragment. These calculations also underestimate

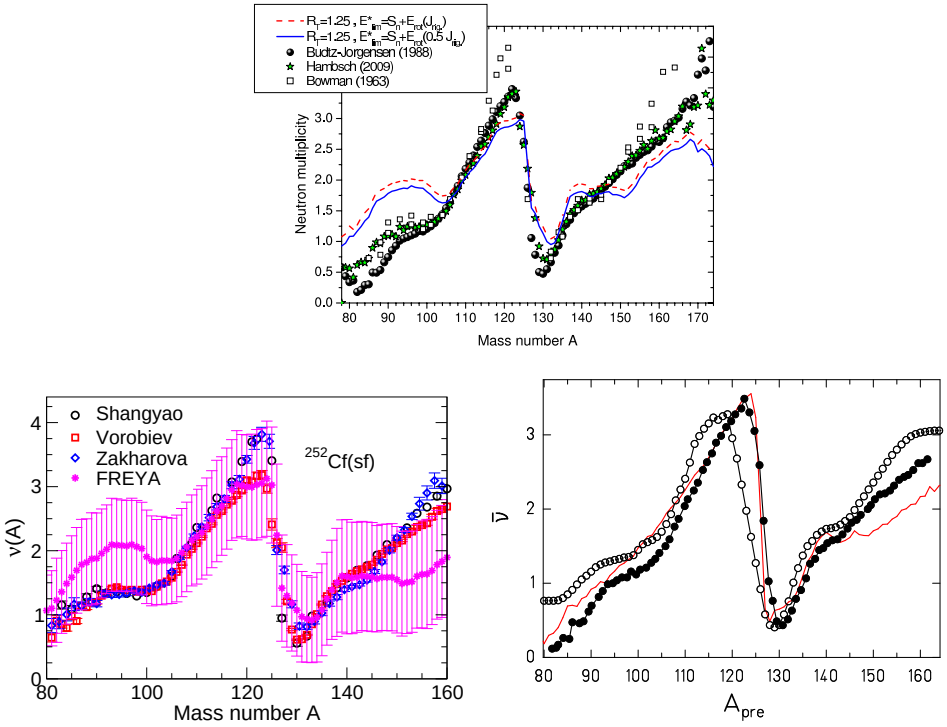

Fig. 11.20 The measured average neutron multiplicity as a function of the fragment mass for ^{252}Cf(sf) compared to results from `FIFRELIN` [103] (*top*), `FREYA` [73] (*bottom left*), and `GEF` [104] (*bottom right*). `FIFRELIN` is compared with data from Refs. [109] (●), [110] (∗), and [47] (□); `FREYA` is compared to data from Refs. [25] (○), [26] (□)and [27] (◊); and `GEF` is compared to the Wahl systematics [108] (○) and data from Ref. [109] (●).

the slope of $\nu(A)$ for the heavy fragment. The `GEF` calculation assumes that the deformation of the fragment shape is given by the same Z dependent function for all fragments.

While there are also several measurements of $\nu(A)$ for neutron-induced fission of ^{239}Pu, the results in the top half of Fig. 11.21, while exhibiting the same general trends, are not in as good agreement as those shown in Fig. 11.20. The agreement between the results of Ref. [100] with $R_T = 1.1$ and `FREYA` with $x = 1.1$ are quite similar. Using an A-dependent value of R_T, obtained by fitting the ratio $\overline{\nu}_L/\overline{\nu}_H$ as a function of A_H to the 1965 Apalin data [22], gives better agreement with $\nu(A)$ near the minimum around $A \sim 130$. Tuning $R_T(A)$ to the ratio of multiplicities, however, does not give overall excellent agreement with the data, even those data it has been extracted from.

As a further check, it is possible to compare the average neutron kinetic energy of the model calculation to the Tsuchiya data [20], the only experiment that reported such data. The results are shown in the bottom panels of Fig. 11.21. Neither $R_T = 1.1$ nor $R_T(A)$ compare as well to these data as to $\nu(A)$. Indeed, the fitted

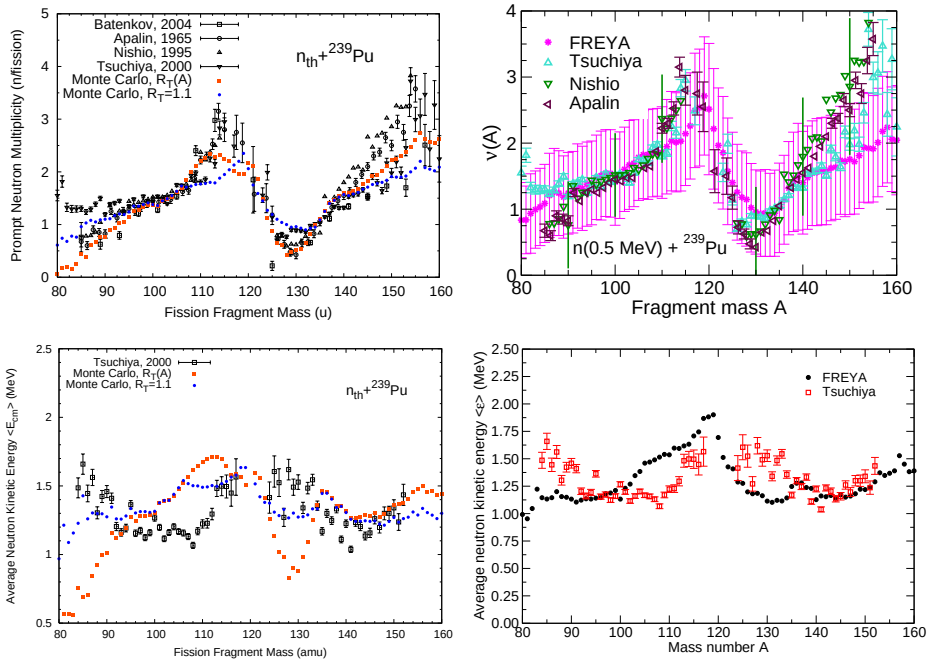

Fig. 11.21 *Top:* Average neutron multiplicity as a function of fragment mass number for ^{239}Pu(n,f): FFD results [100] and data from Batenkov [111] (□), Apalin [22] (○), Nishio [21] (△), and Tsuchiya [20] (▽) (*left*); FREYA results [73] compared with data from Tsuchiya [20] (△), Nishio [21] (▽), and Apalin [22] (◁)(*right*). *Bottom:* Average neutron kinetic energy for ^{239}Pu(n,f): FFD results [100] (*left*) and FREYA results (●) (*right*) compared with data from Tsuchiya [20] (□ and □).

result for $R_T(A)$ gives a dip in the neutron kinetic energy at the same value of A as the dip in the sawtooth, presumably because the lower temperature required by the fit at this point considerably reduces the available kinetic energy near the closed shell. FIFRELIN results on ^{252}Cf(sf) with an A-dependent R_T show an even sharper dip at $A \approx 132$ than the FFD code while the Cf data have a peak in the average neutron kinetic energy at the same region [103]. The FREYA result in the bottom right panel of Fig. 11.21 is similar to the FFD $R_T = 1.1$ result albeit without the sharp cusp in the result of Ref. [100] near $A \approx 105$. FREYA still shows an overestimate in the neutron kinetic energy near $A \approx 110$ and an underestimate near $A \approx 125$.

We now present results for the neutron multiplicity distribution, averaged over fragment mass, first described in Sect. 11.2.3.2. Figure 11.22 shows the neutron multiplicity distribution $P(\nu)$ for ^{239}Pu(n,f) from Refs. [100, 30]. In both cases, the results are compared to the compilation of data presented by Holden and Zucker [44]. Like the data, the model results are considerably different from what could be obtained with Poisson statistics. Again, the results with the fixed, A-independent, values of R_T and x give very similar results, both peaking slightly higher than the

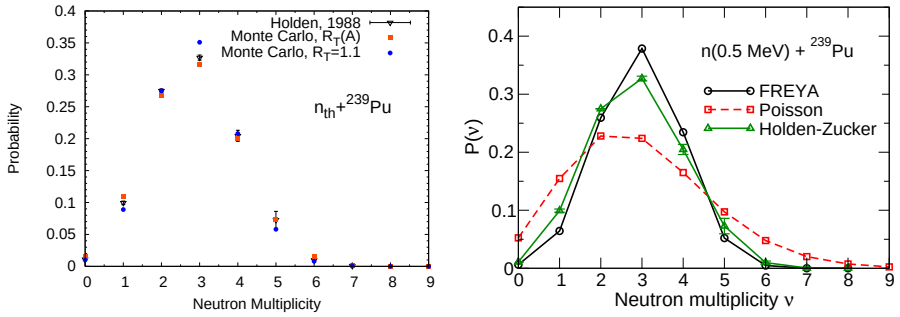

Fig. 11.22 Neutron multiplicity distribution, $P(\nu)$, for neutron-induced fission of ^{239}Pu [44]. *Left:* `FFD` results obtained for $R_T = 1.1$ (●)and $R_T(A)$ [100] (■). *Right:* `FREYA` results obtained with $x = 1.1$ (○), together with the Poisson distribution having the same average ν (□).

compiled data at $\nu = 3$.

We now turn to the average neutron spectrum of ^{239}Pu($n_{\rm th}$,f). This has been measured by a number of experiments and provides an important calculational benchmark. Figure 11.23 shows the ratio of the `FFD` code to a Maxwell distribution with the same temperature as previously shown in Fig. 11.12. In this case the uncertainties in the data are not shown. Two data sets (not shown earlier) by Bojcov [112] and Lajtai [113], both from the mid 1980's, emphasize the differences in the measurements for outgoing neutron energies $E_n < 0.1$ MeV. The results from `FFD` are between the two measurements. They are also somewhat higher than the Los Alamos model-based calculation in the release of the major database, ENDF/B-VII.0 [29]. The ratio is insensitive to R_T, except in the high energy tail of the spectrum ($E_n > 10$ MeV) where $R_T(A)$ becomes considerably harder, which can likely be attributed to the lower neutron kinetic energies near $A \approx 130$. Thus the authors of Ref. [100] conclude that fitting R_T as a function of A should not be considered as giving the 'best' fit but rather more indicative of uncertainties stemming from limitations of the model.

Finally, Fig. 11.24 shows a `FIFRELIN` result related to photon emission. Although none of the recent Monte Carlo models have yet published direct results on photon emission, work is in progress and may be expected soon. Assuming that photon emission only begins after neutron emission has ceased, the residual excitation energy of the fragments after all neutrons have been emitted is a measure of how much energy is available for photon emission. The `FIFRELIN` calculation is compared to Nifenecker's result for $E_\gamma(A_L)$ shown in Fig. 11.14 [103]. While the calculated result is generally independent of A_L for $A_L < 114$, it does jump up by nearly 1 MeV closer to the symmetry value of $A_L = 126$. More detailed comparison of the model with direct photon emission is necessary to determine whether the basic level of agreement holds. New measurements are also needed to ascertain whether the data are correct, given their disagreement with the other measurements

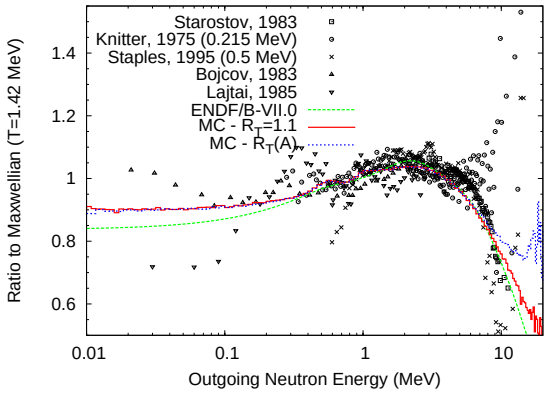

Fig. 11.23 The ratio of the neutron spectrum obtained with the FFD code relative to a Maxwell distribution with T=1.42 MeV for ^{239}Pu($n_{\rm th}$,f). The data shown are from Refs. [57, 58, 112–114]. In addition to the calculated FFD ratios (solid and dotted curves for $R_T = 1.1$ and $R_T(A)$ respectively), the result in the ENDF/B-VII.0 database is presented in the dashed curve.

shown in Fig. 11.14.

A way to correlate photon and neutron emission is to measure the average photon energy as a function of the neutron multiplicity, demonstrating the dependence of the average residual excitation energy in those post-evaporation product nuclei on ν. Because this energy is available for subsequent photon emission, one may expect that the resulting photon multiplicity would display a qualitatively similar behavior and thus, in particular, be anti-correlated with the neutron multiplicity. The FREYA result for ^{252}Cf(sf) is shown on the right-hand side of Fig. 11.24. A similar result was obtained in Ref. [72]. The average residual excitation energy at the average neutron multiplicity, $\overline{\nu} \approx 3.75$, is about 5.3 MeV with a dispersion of about 2 MeV. The average is $\approx$ 1.5 MeV lower than the Nifenecker result but consistent within the uncertainties of the Nardi measurement, see Fig. 11.14. As shown in Ref. [73], there is little sensitivity of the residual excitation to the identity of the fissioning nucleus, suggesting that the energy remaining after prompt neutron emission has ceased is not strongly dependent on the initial fragment temperature.

Phenomenological studies of nuclear fission are of interest for possible practical applications for nonproliferation and security, particularly for the detection of fissile material. New efforts are underway to improve the detection technology, especially for the study of fast fission neutrons. Because fissile material emits neutrons, it is advantageous to utilize these fast neutrons as a signal. Furthermore, correlated neutron observables may be useful for eliminating background sources [115].

We touch on two such correlations here, the spectral shape for various neutron multiplicities and the two-neutron angular correlations. Figure 11.25 show the FREYA results for these observables for spontaneous fission of ^{240}Pu, an important contaminant of enriched ^{239}Pu, and ^{239}Pu(n,f) at E_n = 0.5 and 14 MeV. Com-

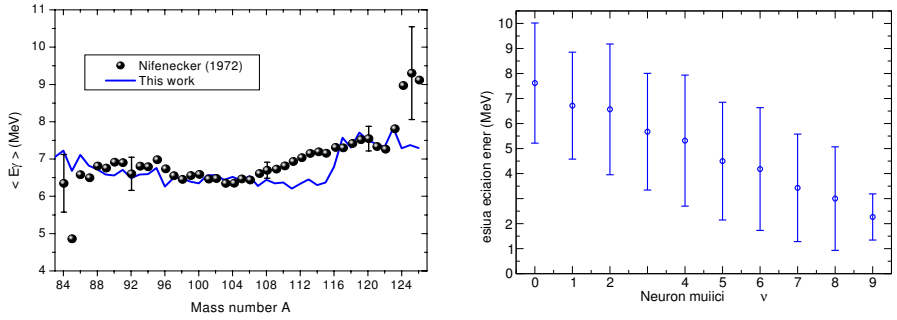

Fig. 11.24 *Left:* The total excitation energy available for photon emission as a function of the light fragment mass, compared to Nifenecker's result [103]. *Right:* The residual excitation energy left in the fragments after neutron emission has ceased, as calculated with `FREYA` [73].

parison of ^{240}Pu(sf) and ^{239}Pu($n_{\rm th}$,f) shows the difference between two systems with the same initial compound nucleus at similar excitation energies, while the difference between results at two different incident neutron energies shows how the correlations depend on E_n.

For fission events with a specified total neutron multiplicity ν, the spectral shape, $f_n^\nu(E) \equiv (1/\nu)d\nu/dE$, is normalized to unity, $\int f_n^\nu(E)dE = 1$. The corresponding spectral shape of neutrons from all the fission events, irrespective of the associated multiplicity, is denoted by $f_n(E)$ and also normalized to unity. Such multiplicity-gated spectral shapes for a variety of cases, calculated with `FREYA`, are shown on the left-hand side of Fig. 11.25 for multiplicities up to $\nu = 6$. It is apparent that the spectra become progressively softer at higher multiplicities, as one would expect because more neutrons are sharing the available energy. This type of elementary conservation-based correlation feature cannot be not provided by the earlier ("standard") models of fission.

The tails of the ^{240}Pu(sf) spectra drop faster and are broader than those from ^{239}Pu($n_{\rm th}$,f). The average energies are also smaller and fewer neutrons are emitted from ^{240}Pu(sf). At $E_n = 14$ MeV, the higher neutron multiplicity means that the spectra for ν up to 6 are more collimated. The average energies are higher, making the spectra harder. There is a clear peak at $E_n - B_n \sim 8.4$ MeV at $\nu = 1$ due to pre-equilibrium emission because this represents the highest available outgoing neutron energy. The high energy tail of the spectrum in this case is all due to first-chance fission with no pre-equilibrium emission. As ν increases, the sharp peak is softened until the average over all ν shows only a relatively small change in slope.

The event-by-event nature of `FREYA` makes it straightforward to extract the angular correlation between two evaporated neutrons, an observable that has long been of experimental interest (see, for example, Refs. [50, 116, 117] and references therein) but which cannot be addressed with the standard models of fission. The right-hand side of Fig. 11.25 shows this quantity for neutrons with kinetic energies

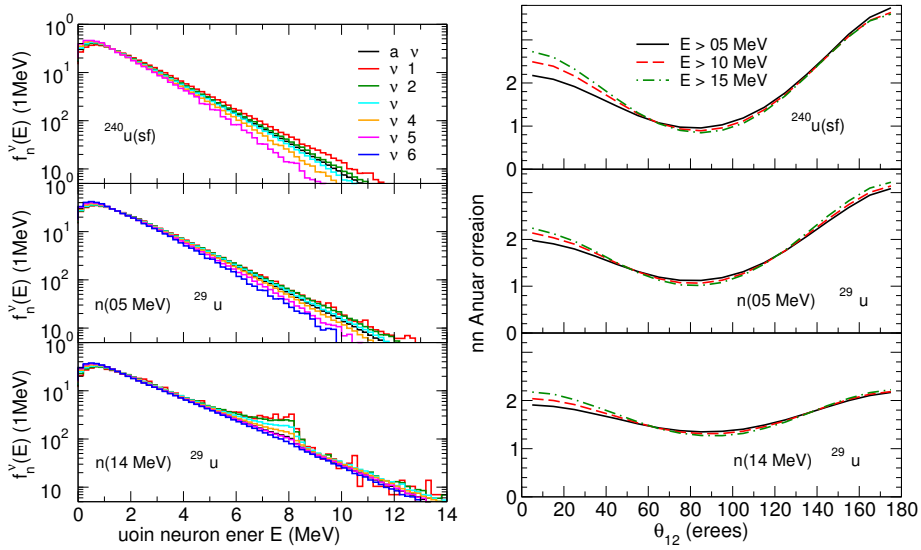

Fig. 11.25 *Left:* The multiplicity-gated spectral distributions for neutrons emitted in association with fission of plutonium: ^{240}Pu(sf) (top), $n(0.5\,\mathrm{MeV})+^{239}$Pu (middle), and $n(14\,\mathrm{MeV})+^{239}$Pu (bottom), for specified neutron multiplicities $\nu = 1-6$ or any ν. *Right:* The corresponding angular correlation between two neutron having a minimum energy of either 0.5 MeV (solid), 1.0 MeV (dashed), or 1.5 MeV (dot-dashed). Calculated with `FREYA` (see Refs. [30, 73]).

above $E = 0.5$, 1 and 1.5 MeV. The angular modulation grows somewhat more pronounced as the threshold is raised while the statistics are correspondingly reduced.

The neutrons tend to be either forward or backward correlated. The backward correlation appears to be somewhat favored. There is a significant correlation at $\theta_{12} = 0$ when both neutrons are emitted from the same fragment, with a higher peak when both neutrons are emitted from the light fragment due to its higher velocity. On the other hand, when one neutron is emitted from each fragment, their direction tends to be anti-correlated due to the relative motion of the emitting fragments, resulting in a peak at $\theta_{12} = 180$. The overall result is a stronger backward correlation because emission of one neutron from each fragment is most likely.

The backward correlation is strongest when the overall neutron multiplicity is low, especially for ^{240}Pu(sf) whereas large multiplicities, reduce the angular correlation. The correlation is already weaker for ^{239}Pu(n_{th},f) with $E_n = 0.5$ MeV because the average neutron multiplicity increases from $\nu \approx 2.15$ for ^{240}Pu(sf) to 2.88 for ^{239}Pu(n_{th},f). For $E_n = 14$ MeV, $\nu \approx 5$ and the forward-backward correlation has nearly vanished, resulting in a more isotropic emission pattern.

11.4 New experiments

Experimental fission research is currently experiencing rapid developments in both capabilities and scope and we give here just a few highlights.

11.4.1 *New fission modes*

Low-energy fission is significantly influenced by nuclear structure effects and therefore offers opportunities for gaining new insights into basic nuclear physics. However, until recently, such low-energy fission studies were limited to nuclei from around thorium to fermium using spontaneous fission, fission induced by thermal neutrons, or β-delayed fission. As we have shown, asymmetric fission dominates over symmetric fission for most isotopes of these elements due to the strong shell effect of the doubly magic nucleus ^{132}Sn. About a decade ago, a new technique developed at GSI [127], Coulomb-excited fission of radioactive beams, made it possible to study low-energy fission in other regions of the nuclear chart. A seminal experiment [127] measured the fragment mass yields from seventy short-lived radioactive nuclei, most of them not formerly accessible, revealing that asymmetry gives way to symmetry for the lighter isotopes of elements below uranium, consistent with earlier studies of stable nuclei [128].

Another way to study low-energy fission in radioactive nuclei is through β-delayed fission (see Ref. [129]), pioneered at Dubna in 1966 [130]. Because the fissioning nucleus results from β decay, its excitation energy is upwards bounded by the associated Q-value. Therefore, given that only final states above the fission barrier may fission, the possible fission events arise from a relatively narrowly defined region of excitation, an advantage relative to electromagnetically induced fission where the excitation has a large spread. Using this technique at ISOLDE (CERN), Andreyev *et al.* [131] studied ^{180}Tl(βdf) and obtained the mass-energy distribution of fission fragments from ^{180}Hg, shown in Fig. 11.26 (*left*). The mass yield is asymmetric, in contrast to widely held expectations based on simple Q-value considerations, because a symmetric split would yield ^{90}Zr which, with $N = 50$ and $Z = 40$, has a negative shell energy, in contrast to the ground states of asymmetric partners. However, this unexpected result can readily be understood by inspecting the potential-energy surface [132], shown in Fig. 11.26 (*right*): Although energetically favorable, a symmetric split is made inaccessible by a potential ridge that causes the shape to develop a sizable asymmetry before scission occurs. This was subsequently confirmed by transport calculations on the same surface [133].

This unexpected discovery has opened up a new region for fission study. Indeed, survey calculations suggest the existence of additional interesting cases in the region of neutron-deficient isotopes of elements below lead [134]. As a result, preparations are underway at JAEA to search for further new asymmetric fission modes for elements between tungsten and gold [135].

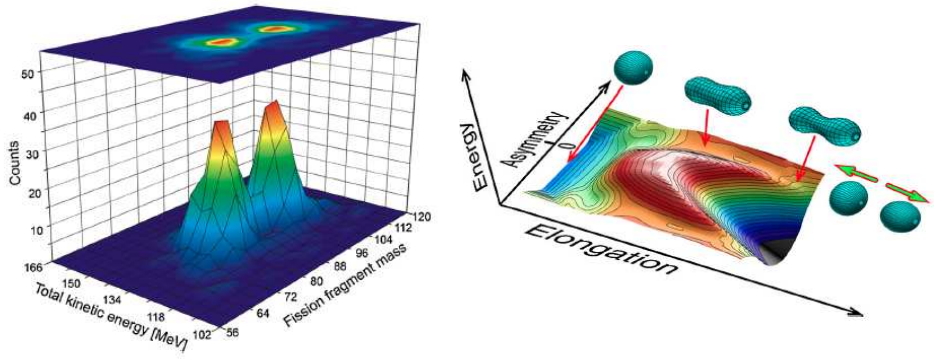

Fig. 11.26 Fission of ^{180}Hg: *Left:* The fragment mass-energy distribution reported in Ref. [131]. *Right:* The potential-energy surface in two dimensions (elongation and asymmetry) resulting from a five-dimensional analysis. Also shown are the shapes for the ground state, the saddle point, the disappearance of the asymmetric valley, and the most likely split. Adapted from Ref. [131].

11.4.2 *New data for applications*

Information on multiplicity and spectra of prompt fission neutrons is crucial for understanding neutron transport in nuclear reactors. In addition, prompt photon emission can contribute up to ten percent of the total energy production in the core of a nuclear reactor, generating substantial heat close to the core. Because most of the rather sparse experimental data are taken only with thermal neutrons and on the major isotopes, ^{235}U(n,f) and ^{239}Pu(n,f), precise nuclear data are needed to model reactor systems that involve 'fast' neutrons, $E_n \approx 1-2$ MeV, and other fissionable isotopes for which data are rarely available. To fill these gaps, both improved modeling, such as by the Monte Carlo methods discussed above, and new experimental efforts are important. The International Atomic Energy Agency (IAEA) has initiated a Coordinated Research Project on Prompt Fission Neutron Spectra of Actinides [118] and the Nuclear Energy Agency of the Organization for Economic Co-operation and Development (OECD) has made a high priority request for new measurements of prompt fission photon measurements [119]. Other efforts are underway that address fission fragment and fission neutron measurements. We briefly describe below a few of the planned measurements.

11.4.2.1 *Fission fragments*

Many nuclear fission applications rely on nuclear data library compilations of fission cross sections and particle kinematics that are based on a combination of experimental results and modeling. Uncertainties in these libraries propagate into the applications. To improve the libraries, in particular by reducing the current level of uncertainties, requires high precision measurements, especially correlating emitted particles such as neutrons and photons with fission fragments at neutron

energies beyond thermal. A new method for measuring fission fragments based on high-energy physics technology, the fission TPC, is being employed for a new set of measurements. A TPC (time-projection chamber) provides a complete, three-dimensional picture of the ionization deposited in a gas (or liquid) volume with a fast, all-electronic read-out. Because a TPC can localize charged particles within a volume, it is extremely useful for identifying particles, in this case fission fragments, through their ionization energy loss.

The fission TPC will first perform fission measurements relative to elastic scattering of neutrons on a hydrogen gas, the gas ultimately planned for filling the chamber. The ^{235}U(n,f) cross section, used as a normalization standard for many measurements, will be determined with a planned uncertainty of less than one percent. The TPC collaboration will first measure the cross section ratios ^{239}Pu(n,f)/^{235}U(n,f) and ^{238}U(n,f)/^{235}U(n,f) as well as the baseline ratio ^{235}U(n,f)/$p(n,n)p$ which will provide the best single measurement of ^{235}U(n,f) and also allow the conversion of other ratios of fission cross sections relative to ^{235}U to absolute measurements [120]. After the initial ratio measurements, the fission fragment distributions, such as TKE(A_H), will be measured for other fissionable nuclei.

11.4.2.2 *Neutron spectra*

The experimental database of fission neutron spectra is very incomplete and most recent libraries are based on the Los Alamos model which uses an average (multiplicity-independent) spectrum. To test the validity of these models and to provide improved data for applications, the Chi-Nu detector [121] is being built to measure the fission neutron spectrum as a function of the incident neutron energy using the spallation neutron source at the Los Alamos Neutron Science Center. The energies of both the incident neutrons, from the spallation source, and those emitted during the fission event are measured. The clock for each event is started by detecting the fission fragment in a low-mass, gas-filled, multi-foil fission chamber [122]. Two neutron detector arrays have been developed; one based on liquid organic scintillators for neutrons with kinetic energies from 600 keV to greater than 10 MeV and the other based on ^{6}Li glass scintillators for neutrons with kinetic energies from 50 keV to $\sim$ 1 MeV. The overlapping energy coverage allows good measurements in the low energy region which is of special interest for applications.

The Institute for Reference Materials and Measurements (IRMM) at Geel, Belgium, is building a neutron detector array based on liquid and crystal scintillator detectors. The crystals, in particular, have a lower neutron detection threshold combined with high detection efficiency [123]. Measurements will be made, in concert with a time-of-flight spectrometer, for low energy neutrons on ^{235}U(n,f) and ^{239}Pu(n,f).

11.4.2.3 *Fission yields*

As we discussed in Sect. 11.1.2, the measured fission product yields $Y(A)$ may depend on the initial energy. In nuclear test data, certain products with high yields, such as ^{147}Nd, are utilized to determine the explosive yield. Because such data include a range of energies, it is important to study the dependence of $Y(A)$ on E_n. In addition, such studies provide quality data for testing theoretical calculations of fission yields, such as those discussed in Sect. 11.3.1.

Because previous extractions of fission yields by different groups remain a point of contention, a new set of precision measurements is required to resolve these long-standing differences and determine the correct fission product yields for analysis of nuclear test data. A new experiment at the Triangle Universities Nuclear Laboratory (TUNL) will undertake a complete, high-precision, self-consistent study of the dependence of $Y(A)$ on incident neutron energy. The required precision is obtained by employing relative measurement techniques, making yield ratios in which a number of less well determined quantities, such as the number of incident neutrons, cancel, reducing systematic uncertainties.

At TUNL, deuterons from the Tandem Van de Graaff are used to produce quasi-monoenergetic neutron beams via reactions such as $\mathrm{d} + \mathrm{d} \rightarrow n + \mathrm{t}$, with neutron energies E_n up to 16 MeV. In the experiments, the resulting collimated neutron beam, with a flux of $10^7/cm^2$, is directed on a thin (several hundred μm) actinide sample, such as ^{235}U, ^{238}U, or ^{239}Pu, placed within a double-sided fission proportional chamber furnished with very thin fission foils. The sample is typically irradiated for 24 hours. When the sample is removed, photons emitted from the irradiated assembly are counted offline with a precision photon spectrometer. The discrete energies of these photons are used to identify the emitting fission product nucleus. A new actinide sample is introduced into the proportional chamber and the cycle is repeated with a new value of E_n until the energy scan for the given actinide is complete. Because the proportional counter and fission foils are unchanged, the photon yields at a given E_n can be normalized to the incident neutron flux obtained by the fission counter. The geometry of the counter cancels in the yield ratio, allowing the precision measurements necessary.

11.4.2.4 *Photon measurements*

The IRMM has also investigated novel scintillator systems, such as lanthanum (III) bromide, lanthanum (III) chloride, and cerium (III) bromide, to measure fission photons. These inorganic scintillators combine a high light yield with the best available energy resolution. The timing resolution should be up to an order of magnitude better than sodium-iodide technology. These systems promise to improve our understanding of prompt photon emission in fission [124–126] which is overdue. The IRMM measurements will focus on correlating photon energy and multiplicity with fission fragment mass and total kinetic energy, as in Figs. 11.14 and 11.15.

11.5 Concluding remarks

Fission has a long and complex history. What started out as an interesting quest for basic science in a few laboratories in the early days of quantum mechanics and nuclear physics remarkably quickly became focused on practical applications.

The simple fact that a large nucleus splits apart after neutron absorption, releasing a large amount of energy while also emitting several neutrons, makes an energy producing chain reaction possible. When controlled, such a fission chain reaction can be harnessed to produce energy and may thus be of significant benefit to society. Furthermore, and very importantly, a run-away fission chain reaction, when carefully orchestrated, may released unprecedented amounts of energy in a very short time, offering obvious military applications.

The focus on certain isotopes of key importance for explosives has, however, tended to concentrate much of the research on certain narrow areas, allowing other aspects of the field to languish. But new applications of fission phenomena, such as detection of fissionable material, accelerator-driven systems, new electro-nuclear power cycles, and the new exotic beam facilities, have stimulated renewed scientific interest. These developments have also brought attention to the dearth of data and it can be expected that new experiments, utilizing modern techniques, may soon be able to fill some of these gaps.

Nuclear fission is a non-equilibrium process in a mesoscopic system and thus it involves many subjects at the modern frontier. We have shown that, far from being a well understood phenomenon, fission physics is still an active area of research where important new work still waits to be done. While new approximation techniques have made it possible to determine the fission yields rather accurately on the basis of the calculated potential energy surface of the nucleus as it approaches scission, the improved availability of large-scale computer resources have made microscopic quantum-mechanical treatments of fission more tractable, although additional formal developments are still needed. On the phenomenological side, which we have particularly illuminated here, modern Monte Carlo treatments that provide large samples of complete fission events are making it possible, for the first time, to address arbitrary combinations of observables simultaneously, thus making it possible to gain improved physical insight from the experimental data.

Acknowledgments. We wish to acknowledge helpful discussions with and information from J.A. Becker, A. Bernstein, D.L. Bluel, A. Chyzh, F.-J. Hambsch, M. Heffner, H.J. Krappe, D. McNabb, P. Möller, E.B. Norman, K.-H. Schmidt, O. Serot, A.J. Sierk, P. Talou, and C.-Y. Wu. This work was supported by the Office of Nuclear Physics in the U.S. Department of Energy's Office of Science under Contracts No. DE-AC52-07NA27344 (RV) and DE-AC02-05CH11231 (JR).

Bibliography

[1] R. Rhodes, *The Making of the Atomic Bomb*, Simon & Schuster, New York, 1986.
[2] A. Pais, *Niels Bohr's Times*, Clarendon Press, Oxford, 1991.
[3] E. Rutherford, Phil. Mag. **21**, 669 (1911).
[4] J. Chadwick, Nature **129**, 312 (1932).
[5] E. Fermi, E. Amaldi, O. D'Agostino, F. Rasetti, and E. Segre, Proc. Roy. Soc. **452**, 483 (1934).
[6] I. Noddack, Z. Angewandte Chemie **47**, 653 (1934).
[7] O. Hahn and F. Strassmann, Naturwiss. **27**, 11 (1939).
[8] L. Meitner and O.R. Frisch, Nature **143**, 239 (1939).
[9] G. Gamow, *Constitution of nuclei and radioactivity*, Oxford University Press, 1931.
[10] N. Bohr: Nature **137**, 344 (1936).
[11] A. Einstein, Ann. Physik **17**, 891 (1905).
[12] O.R. Frisch, Nature **143**, 276 (1939).
[13] H. von Halban, Jun., F. Joliot, and L. Kowarski, Nature **143**, 680 (1939).
[14] L. Meitner and O.R. Frisch, Nature (London) **143**, 239 (1939).
[15] N. Bohr, Nature (London) 143, **330** (1939).
[16] N. Bohr and J.A. Wheeler, Phys. Rev. 56, 426 (1939).
[17] M. Bolsterli, E.O. Fiset, J.R. Nix, J.L. Norton, Phys. Rev. C **5**, 1050 (1972).
[18] P. Möller, J.R. Nix, W.D. Myers, and W.J. Swiatecki, At. Data Nucl. Data Tables **59**, 185 (1995).
[19] T.R. England and B.F. Rider, LA-UR-94-3106 (1994).
[20] C. Tsuchiya, Y. Nakagome, H. Yamana, H. Moriyama, K. Nishio, I. Kanno, K. Shin, and I. Kimura, J. Nucl. Sci. Technol. **37**, 941 (2000), EXFOR entry 22650-003, 22650-005.
[21] K. Nishio, Y. Nakagome, I. Kanno, and I. Kimura, J. Nucl. Sci. Technol. **32**, 404 (1995), EXFOR entry 23012-005, 23012-006.
[22] V.F Apalin, Yu.N. Gritsyuk, I.E. Kutikov, V.I. Lebedev, and L.A. Mikaelian, Nucl. Phys. A **71**, 553 (1965), EXFOR entry 41397-002.
[23] E. E. Maslin and A. L. Rodgers, Phys. Rev. **164**, 1520 (1967).
[24] K. Nishio, Y. Nakagome, H. Yamamoto, and I. Kimura, Nucl. Phys. A **632**, 540 (1998).
[25] D. Shengyao, X. Jincheng, L. Zuhua, L. Shaoming, and Z. Huanqiao, Chin. Phys. **4**, 649 (1984).
[26] V.N. Dushin, F.J. Hambsch, V.A. Yakovlev, V.A. Kalinin, I.S. Kraev, A.B. Laptev, D.V. Nikolav, B.F. Petrov, G.A. Petrov, V.I. Petrova, Y.S. Pleva, O.A. Shcherbakov, V.I. Shpakov, V.E. Sokolov, A.S. Vorobiev, T.A. Zavarukhina, Nucl. Instrum. Meth.

A **516**, 539 (2004).
[27] V.P. Zakharova, D.K. Ryazanov, B.G. Basova, A.D. Rabinovich, V.A. Korostylev, Sov. J. Nucl. Phys. **30**, 19 (1979).
[28] P. Fröbrich and I.I. Gontchar, Phys. Reports **292**, 131 (1998(.
[29] M.B. Chadwick *et al.*, Nucl. Data Sheets **107** (2006) 2931.
[30] R. Vogt, J. Randrup, D.A. Brown, M.A. Descalle, and W.E. Ormand, Phys. Rev. C **85**, 024608 (2012).
[31] W.J. Swiatecki, K. Siwek-Wilczynska, and J. Wilczynski, Phys. Rev. C **78**, 054604 (2008).
[32] J. Randrup and R. Vogt, Phys. Rev. C **80**, 024601 (2009).
[33] T. Kawano, T. Ohsawa, M. Baba, and T. Nakagawa, Phys. Rev. C **63**, 034601 (2001).
[34] E. Gadioli, P.E. Hodgson, *Pre-equilibrium Nuclear Reactions*, Oxford Univ. Press, New York, 1992.
[35] R. Schmidt and H. Henschel, Nucl. Phys. A **395**, 15 (1983).
[36] G.F. Knoll, *Radiation detection and measurement* (3rd ed., 1999), New York: Wiley, ISBN 0-471-07338-5.
[37] D.R. Nygren, eConf C **740805**, 58 (1974); D. Fancher, H.J. Hilke, S. Loken, P. Martin, J.N. Marx, D.R. Nygren, P. Robrish, and G. Shapiro, M. Urban, W. Wenzel, W. Gom, and J. Layter, Nucl. Instrum. Meth. **161**, 383 (1979).
[38] W. Reisdorf, J.P. Unik, H.C. Griffin, and L.E. Glendenin, Nucl. Phys. A **177**, 337 (1971).
[39] C. Wagemans, E. Allaert, A. Deruytter, R. Barthélémy, and P. Schillebeeckx, Phys. Rev. C **30**, 218 (1984), EXFOR entry 21995-038.
[40] F.-J. Hambsch and S. Oberstedt, Nucl. Phys. A **617**, 347 (1997).
[41] P. Schillebeeckx, C. Wagemans, A.J. Deruytter, and R. Barthelemy, Nucl. Phys. A **545**, 623 (1992).
[42] M.P. Ivanov, G.M. Ter-akopian, B.V. Fefilov, and A.S. Voronin, Nucl. Inst. Meth. A **234**, 152 (1985).
[43] B.D. Wilkins, E.P. Steinberg, and R.R. Chasman, Phys. Rev. C **14**, 1832 (1976).
[44] N.E. Holden and M.S. Zucker, "A Reevaluation of the Average Prompt Neutron Emission Multiplicity ($\overline{\nu}$) Values from Fission of Uranium and Transuranium Nuclides", BNL-NCS-35513, Brookhaven National Laboratory (1985).
[45] Z. Huanqiao, L. Zuhua, D. Shengyao and L. Shaoming, Nucl. Sci. Eng. **86**, 315 (1984).
[46] J.W. Boldeman, *Second Conference on Neutron Physics*, **4**, 114 (1973), EXFOR entry 30376-006.
[47] H.R. Bowman, J.C.D. Milton, S.G. Thompson, and W.J. Swiatecki, Phys. Rev. **126**, 2120 (1962); Phys. Rev. **129**, 2133 (1963).
[48] A.S. Vorobiev, V.N. Dushin, F.J. Hambsch, V.A. Yakovlev, V.A. Kalinin, I.S. Kraev, A.B. Laptev, B.F. Petrov, G.A. Petrov, Yu.S. Pleva, O.A. Shcherbakov, and V.E. Sokolov, EXFOR entry 41425-004.
[49] A.S. Vorobiev, V.N. Dushin, F.J. Hambsch, V.A. Yakovlev, V.A. Kalinin, I.S. Kraev, A.B. Laptev, B.F. Petrov, G.A. Petrov, Yu.S. Pleva, O.A. Shcherbakov and V.E. Sokolov, EXFOR entry 41425-002.
[50] C.B. Franklyn, C. Hofmeyer, and D.W. Mingay, Phys. Lett. B **78**, 564 (1978).
[51] J.W. Boldeman, A.R. de'L. Musgrove, and R.L. Walsh, Aust. J. Phys. **24**, 821 (1971).
[52] B.C. Diven, H.C. Martin, R.F. Taschek, and J. Terrell, Phys. Rev. **101**, 1012 (1956).
[53] J. Błocki, Y. Boneh, J.R. Nix, J. Randrup, M. Robel, A.J. Sierk, and W.J. Swiatecki,

Ann. Phys. **113**, 330 (1978).
[54] D.G. Madland, Nucl. Phys. A **772**, 113 (2006).
[55] D. Abramson and C. Lavelaine, A.E.R.E. Harwell Rep. No. 8636 (1977), EXFOR entry 20997-004.
[56] V.N. Nefedov, B.I. Starostov, and A.A. Bojcov, "6$^{\text{th}}$ All-Union Conf. on Neutron Physics", Kiev, Ukraine (1983) Vol. 2, p. 285, EXFOR entry 40871-009.
[57] H. Knitter, Atomkernenerg. **26**, 76 (1975), EXFOR entry 20576-003.
[58] P. Staples, J.J. Egan, G.H.R. Kegel, A. Mittler, and M.L. Woodring, Nucl. Phys. A **591**, 41 (1995), EXFOR entry 13982-003.
[59] J.M.'Adams and P.I. Johansson, Conf. on Nucl. Cross Sect. and Techn., Washington 1975, Vol. 2, p. 631, EXFOR entry 20996-003.
[60] H. Conde, G. During, and J. Hansen, Arkiv för Fysik **29**, 307; 313 (1965), EXFOR entry 20575-003, 20575-004.
[61] G.S. Boikov, V.D. Dmitriev, G.A. Kudyaev, M.I. Svirin, and G.N. Smirenkin, At. Energ. **69**, 23 (1990), EXFOR entry 41904-003.
[62] F. Pleasonton, R.L. Ferguson, and H.W. Schmitt, Phys. Rev. C **6**, 1023 (1972).
[63] H. Nifenecker, C. Signarbieux, M. Ribrag, J. Poitou, and J. Matuszek, Nucl. Phys. A **189**, 285 (1972).
[64] E. Nardi, A. Gavron, and Z. Fraenkel, Phys. Rev. C **8**, 2293 (1973).
[65] J.B. Wilhelmy, E. Cheifetz, R.C. Jared, S.G. Thompson, H.R. Bowman, and J.O. Rasmussen, Phys. Rev. C **5**, 2041 (1972).
[66] M.M. Hoffman, Phys. Rev. **133**, B714 (1964).
[67] A. Chyzh *et al.*, Phys. Rev. **85**, 02160(R) (2012).
[68] M. Heil *et al.*, Nucl. Instr. Meth. A **459**, 229 (2001).
[69] D.L. Bleuel *et al.*, Nucl. Instr. Meth. A **624**, 691 (2010).
[70] C.Y. Wu *et al.*, Nucl. Instr. Meth. A **694**, 78 (2012).
[71] G. S. Brunson Jr., LA-940B-T (1982).
[72] S. Lemaire, P. Talou, T. Kawano, M.B. Chadwick, and D.G. Madland, Phys. Rev. C **73**, 014602 (2006).
[73] R. Vogt and J. Randrup, Phys. Rev. C **84**, 044621 (2011).
[74] H.J. Krappe and K. Pomorski, *Theory of Nuclear Fission*, Springer-Verlag, Berlin 2012, ISBN 978-3-642-23514-6.
[75] A. Einsten, Annalen der Physik **326**, 756 (1906).
[76] M. von Smoluchowski, Annalen der Physik **322**, 549 (1905).
[77] M. Brack, J. Damgaard, A.S. Jensen, H.C. Pauli, V.M. Strutinsky, and C.Y. Wong, Rev. Mod. Phys. **44**, 320 (1972).
[78] J.R. Nix, Nucl. Phys. A **130**, 214 (1969).
[79] P. Möller, D.G. Madland, A.J. Sierk, and A. Iwamoto, Nature **409**, 785 (2001).
[80] P. Möller, A.J. Sierk, T. Ichikawa, A. Iwamoto, R. Bengtsson, H. Uhrenholt, and S. Åberg, Phys. Rev. C **79**, 064304 (2009).
[81] H. Hofmann, *The Physics of Warm Nuclei: with Analogies to Mesoscopic Systems*, Oxfor Scholarship Online, 2008
[82] A.J. Sierk and J.R. Nix, Phys. Rev. C **21**, 982 (1980).
[83] W.U. Schröder, J.R. Birkelund, J.R. Huizenga, W.W. Wilcke, and J. Randrup, Phys. Rev. Lett. **44**, 308 (1980).
[84] W.U. Schröder and J.R. Huizenga, *Damped Nuclear Reactions*, in *Treatise on Heavy-Ion Science*, Plenum Press, *Ed.* D.A. Bromley, Vol. 2, pp. 113-726 (1984).
[85] C. Schmitt, J. Bartell, K. Pomorski, and A, Surowiec, Acta Phys. Pol. B **34**, 1651 (2002).
[86] C. Schmitt, J. Bartell, A. Surowiec, and K. Pomorski, Acta Phys. Pol. B **34**, 2135

(2002).
[87] G.D. Adeev, A.V. Karpov, P.N. Nadtochii, and D.V. Vanin, Phys. Part. Nucl. **36**, 378 (2005).
[88] P.N. Nadtochy, E.G. Ryabov, A.E. Gegechkori, Yu.A. Anischenko, and G.D. Adeev, Phys. Rev. **85**, 064619 (2012).
[89] J. Randrup and P. Möller, Phys. Rev. Lett. **106**, 132503 (2011).
[90] J. Randrup, P. Möller, and A.J. Sierk, Phys. Rev. C **84**, 034613 (2011).
[91] P. Fong, Phys. Rev. 102, 434 (1956).
[92] B.D. Wilkins, E.P. Steinberg, and R.R. Chasman, Phys. Rev. C 14, 1832 (1976).
[93] U. Brosa, S. Grossmann, and A. Müller, Phys. Rep. **97**, 1 (1990);
[94] N. Dubray, H. Goutte, and J.-P. Delaroche, Phys. Rev. C **77**, 014310 (2008).
[95] W. Younes and D. Gogny. Phys. Rev. C **80**, 054313 (2009).
[96] H. Goutte, J.-F. Berger, P. Casoli, and D. Gogny, Phys. Rev. C **71**, 024316 (2005).
[97] D.G. Madland and J.R. Nix, Nucl. Sci. Eng. **81**, 213 (1982).
[98] G. Vladuca and A. Tudora, Ann. Nucl. Energy **28**, 419 (2001); A. Tudora, Ann. Nucl. Energy **36**, 72 (2009).
[99] S. Lemaire, P. Talou, T. Kawano, M.B. Chadwick, and D.G. Madland, Phys. Rev. C **72**, 024601 (2005).
[100] P. Talou, B. Becker, T. Kawano, M.B. Chadwick, and Y. Danon, Phys. Rev. C **83**, 064612 (2011).
[101] R. Vogt, J. Randrup, J. Pruet, and W. Younes, Phys. Rev. C **80**, 044611 (2009).
[102] R. Vogt and J. Randrup, Phys. Rev. C (submitted).
[103] O. Litaize and O. Serot, Phys. Rev. C **82**, 054616 (2010).
[104] K.-H. Schmidt and B. Jurado, JEF/DOC 1423, OECD-NEA (2012).
[105] K.-H. Schmidt and B. Jurado, Phys. Rev. Lett. **104**, 212501 (2010); Phys. Rev. C **82**, 014607 (2011); Phys. Rev. C **83**, 061601 (2011).
[106] V.F. Weisskopf, Phys. Rev. **52**, 295 (1937).
[107] H. Koura, M. Uno, T. Tachibana, and M. Yamada, Nucl. Phys. A **674**, 47 (2000).
[108] A.C. Wahl, At. Data Nucl. Data Tables **39** (1988) 1.
[109] C. Budtz-Jørgensen, H.-H. Knitter, Nucl. Phys. A **490**, 307 (1988).
[110] F.-J. Hambsch, S. Oberstedt, S. Zeynalov, N. Kornilov, I. Fabry, R. Borcea and A. Al-Adili, in *Proceedings of the International Workshop on Compound Nuclear Reactions and Related Topics*, Bordeaux, France, 2009, *Ed.* L. Bonneau *et al.* (EDP Sciences, Les Ulis, France, 2009), p. 07002.
[111] O.A. Batenkov, G.A. Boykov, F.-J. Hambsch, J.H. Hamilton, V.A. Jakovlev, V.A. Kalinin, A.B. Laptev, V.E. Sokolov, and A.S. Vorobyev, AIP Conf. Proc. **769**, 1003 (2004).
[112] A.A. Bojcov, A.F. Semenov, and B.I. Starostov, Proceedings of the 6^{th} All Union Conference on Neutron Physics, Kiev, 2-6 October 1983, p. 294, EXFOR entry 40873-006 (1983).
[113] A. Lajtai, J. Kecsikeméti, J. Sáfár, P.P. Dyachenko, and V.M. Piksaikin, Proceedings of the International Conference on Nuclear Data for Basic and Applied Science, *Eds.* P.G. Young, R.E. Brown, G.F. Auchampaugh, P.W. Lisowski, and L. Stewart (Gordon and Breach, New York, 1985), Vol. 1, p. 613.
[114] B.I. Starostov, V.N. Nefedov, and A.A. Bojcov, *6th All-Union Conf. on Neutron Physics*, Kiev, Ukraine (1983) Vol. 2, p. 290, EXFOR entry 40872-003 (1983).
[115] R.C. Runkle, A. Bernstein and P.E. Vanier, J. Applied Phys. **108**, 111101 (2010).
[116] S. DeBenedetti, J.E. Francis, Jr., W.M. Preston, and T.W. Bonner, Phys. Rev. **74**, 1645 (1948).
[117] A.M. Gagarski *et al.*, Bull. Russ. Acad. Sciences: Physics, **72**, 773 (2008).

[118] http://www-nds.iaea.org/pfns/public.html
[119] http://www.oecd-nea.org/dbdata/hprl/
[120] M. Heffner, AIP Conf. Proc. **1005**, 182 (2008).
[121] R.C. Haight *et al.*, Proceedings of the International Workshop on Fast Neutron Detectors and Applications, Ein Gedi, Israel, J. Instrum., **7** C03028 (2012), doi:10.1088/1748-0221/7/03/C03028
[122] C.Y. Wu *et al.*, LLNL-TR-461044 (2010).
[123] C. Mattei *et al.*, Nucl. Instr. Meth. A **678**, 135 (2012).
[124] R. Billnert *et al.*, Nucl. Instr. Meth. A **647**, 94 (2011).
[125] R. Billnert *et al.*, Phys. Proc. **31**, 29 (2012).
[126] A. Oberstedt *et al.*, Nucl. Instr. Meth. A **668**, 14 (2012).
[127] K.-H. Schmidt *al.*, Nucl. Phys. A **665**, 221 (2000); **693**, 169 (2001).
[128] M.G. Itkis *et al.* Sov. J. Nucl. Phys. **52**, 601 (1990); **53**, 757 (1991).
[129] H.L. Hall and D.C. Hoffman, Ann. Rev. Nucl. Sci. **42**, 147 (1992).
[130] V.I. Kuznetzov and N.K. Skobelev, Yad. Fiz. **4**, 279 (1966); **5**, 271 (1967); **5**, 1136 (1967).
[131] A.N. Andreyev *et al.*, Phys. Rev. Lett. **105**, 252502 (2010).
[132] T. Ichikawa, A. Iwamoto, P. Möller, and A.J. Sierk, Phys. Rev. C **86**, 024610 (2012).
[133] P. Möller, J. Randrup, and A.J. Sierk, Phys. Rev. C **84**, 034613 (2011).
[134] P. Möller and J. Randrup, in preparation (2012).
[135] K. Nishio *et al.*, private communication (2012).